

The clustering of the SDSS-IV extended Baryon Oscillation Spectroscopic Survey DR14 LRG sample: structure growth rate measurement from the anisotropic LRG correlation function in the redshift range $0.6 < z < 1.0$

M. Icaza-Lizaola^{1,2,3*}, M. Vargas-Magaña^{1†}, S. Fromenteau^{4‡}, S. Alam⁵, B. Camacho¹, H. Gil-Marín⁶, R. Paviot⁷, Ashley Ross⁸, Donald P. Schneider^{9,10}, Jeremy Tinker¹¹, Yuting Wang¹², Cheng Zhao¹¹, Abhishek Prakash¹³, G. Rossi¹⁴, Gong-Bo. Zao¹⁵, Irene Cruz-Gonzalez², Axel de la Macorra¹.

¹ Instituto de Física, Universidad Nacional Autónoma de México, Apdo. Postal 20-364, Ciudad de México, Mexico.

² Instituto de Astronomía, Universidad Nacional Autónoma de México, Apdo. Postal 70-264, Ciudad de México, Mexico.

³ Institute for Computational Cosmology, Department of Physics, University of Durham, South Road, Durham DH1 3LE, UK.

⁴ Instituto de Ciencias Físicas, Universidad Nacional Autónoma de México, Av. Universidad s/n, 62210 Cuernavaca, Mor., Mexico.

⁵ Institute for Astronomy, University of Edinburgh, Royal Observatory, Blackford Hill, Edinburgh, EH9 3HJ, UK.

⁶ Institut de Ciències del Cosmos, Universitat de Barcelona ICCUB.

⁷ Aix Marseille Université, CNRS, LAM, Laboratoire d'Astrophysique de Marseille, Marseille, France.

⁸ Center for Cosmology and AstroParticle Physics, The Ohio State University, Columbus, OH 43210, USA.

⁹ Department of Astronomy and Astrophysics, The Pennsylvania State University, University Park, PA 16802.

¹⁰ Institute for Gravitation and the Cosmos, The Pennsylvania State University, University Park, PA 16802.

¹¹ New York University, Center for Cosmology and Particle Physics, Department of Physics, 726 Broadway, Room 1005, New York, NY 10003, USA.

¹² National Astronomy Observatories, Chinese Academy of Science, Beijing, 100101, P.R.China.

¹³ IPAC, California Institute of Technology, MC 100-22, 1200 E California Boulevard, Pasadena, CA 91125, USA.

¹⁴ Department of Physics and Astronomy, Sejong University, Seoul, 143-747, Korea.

¹⁵ Laboratory of Astrophysics, Ecole Polytechnique Fédérale de Lausanne (EPFL), Observatoire de Sauverny, 1290 Versoix, Switzerland.

Accepted XXX. Received YYY; in original form ZZZ

ABSTRACT

We analyze the anisotropic clustering of the Sloan Digital Sky Survey-IV Extended Baryon Oscillation Spectroscopic Survey (eBOSS) Luminous Red Galaxy Data Release 14 (DR14) sample combined with Baryon Oscillation Spectroscopic Survey (BOSS) CMASS sample of galaxies in the redshift range $0.6 < z < 1.0$, which consists of 80,118 galaxies from eBOSS and 46,439 galaxies from the BOSS-CMASS sample. The eBOSS-CMASS Luminous Red Galaxy sample has a sky coverage of $1,844 \text{ deg}^2$, with an effective volume of 0.9 Gpc^3 . The analysis was made in configuration space using a Legendre multipole expansion. The Redshift Space Distortion signal is modeled as a combination of the Convolution Lagrangian Perturbation Model and the Gaussian Streaming Model. We constrain the logarithmic growth of structure times the amplitude of dark matter density fluctuations, $f(z_{\text{eff}})\sigma_8(z_{\text{eff}}) = 0.454 \pm 0.139$, and the Alcock-Paczynski dilation scales which constraints the angular diameter distance $D_A(z_{\text{eff}}) = 1466.5 \pm 136.6(r_s/r_s^{\text{fid}})$ and $H(z_{\text{eff}}) = 105.8 \pm 16(r_s^{\text{fid}}/r_s) \text{ km s}^{-1} \text{ Mpc}^{-1}$, where r_s is the sound horizon at the end of the baryon drag epoch and r_s^{fid} is its value in the fiducial cosmology at an effective redshift $z_{\text{eff}} = 0.72$. These results are in full agreement with the current Λ -Cold Dark Matter (Λ -CDM) cosmological model inferred from Planck measurements. This study is the first eBOSS LRG full-shape analysis i.e. including Redshift-Space Distortions (RSD) simultaneously with the Alcock-Paczynski (AP) effect and the Baryon Acoustic Oscillation (BAO) scale.

Key words: Redshift Space Distortions – Dark Energy – Modified Gravity

1 INTRODUCTION

The standard cosmological model (Λ -CDM) accurately describes most observations. However, the acceleration of the

* E-mail: miguel.a.de-icaza-lizaola@durham.ac.uk

† E-mail: mmaganav@fisica.unam.mx

‡ E-mail: sfroment@icf.unam.mx

expansion of our Universe requires the existence of a dominating source of exotic energy, i.e., the Dark Energy. This energy remains undetected to this day, which has led to many searches for an alternative explanation. One possibility is to modify the geometric part of Einstein's equations, which corresponds to changing the General Relativity (hereafter GR) equations rather than invoking a new component in the stress-energy tensor. A common modification to GR is the addition of a cosmological constant, Λ , coupled to the metric. However, it is not possible to distinguish between Λ and a specific case of Dark Energy with a constant equation of state $w = -1$.

Another way to reproduce cosmological observations is to modify the gravity model. Various alternative gravitational models have been studied during the past 50 years which can be grouped in different families. Extra-field theories, such as $f(R)$ (Sotiriou & Faraoni 2010), Tensor-Scalar theories, extra-dimension theories, such as DGP (Fang et al. 2008), braneworld, and string gravity models, and higher-order theories such as the Galileons model (Joyce et al. 2015) are some of them.

All modified gravity models must recover the GR results at the local scale (i.e., for high density) where GR has been strongly tested; this is generally solved by invoking screening mechanisms. Therefore, any modification has to appear in the context of weak gravity and large scales; this is the reason why cosmology, and more particularly Large-Scale-Structures (LSS) observations, is the appropriate framework for this study.

Cosmological constraints on the theory of gravity are primarily produced from LSS observations, the most important of these being Supernovae (Riess et al. 1998; Perlmutter et al. 1999), Baryon Acoustic Oscillations (Eisenstein et al. 2005; Alam et al. 2017a) and weak lensing (Sheldon et al. 2004), and from the early Universe through Cosmic Microwave Background observations, when the density contrast was of the order of $\sim 10^{-5}$ (Planck Collaboration et al. 2016).

Large-scale peculiar velocities, combined with standard clustering, are a unique framework to distinguish between the various models of gravity. However, making precise measurements on this scale is challenging. The Kinetic Sunyaev-Zel'dovich effect is a possibility (Mueller et al. 2014) but requires measurements of massive galaxy clusters with high precision on the SZ signal estimation. Conversely, we can directly use the imprint of these velocities on the redshift measurement through the Redshift Space Distortions (RSD) in the anisotropic correlation function of galaxies (or other tracers of the dark matter). The measured redshift is the sum of the Hubble flow, the Doppler effect due to the peculiar velocities of the observer and the observed galaxies, and a small contribution from gravitational redshift. If the peculiar velocities are randomly distributed, then they only contribute as a noise. They are, however, correlated with the density field, revealing cosmological information, in particular allowing us to distinguish between dark energy models or deviations from GR. The Redshift Distortion introduces anisotropies in the galaxy-galaxy two-point correlation function, particularly if we stack the information around overdensities, where these tracers live. Performing an anisotropic study, i.e., using the angle with respect to the line-of-sight as a statistical breakdown, we can detect the coherent defor-

mations of the 3D two-point correlation function predicted by the Kaiser (1987) effect.

BAO and supernova measurements are constraints on the expansion history of the Universe. However, it has been shown that an appropriate choice of the equation of state $w(a)$ can allow different cosmological models to have the same expansion history (Linder 2005). In order to break this degeneracy one can complement expansion history observations with the clustering history of the structures through the measurement of the linear growth rate:

$$f(a) = \frac{d \ln D(a)}{d \ln a}, \quad (1)$$

where $D(a)$ is the linear growth factor as a function of the scale factor a , and it quantifies the degree of structure at that time. In this paper we extend the growth rate f measurement from previous surveys to an effective redshift of $z = 0.72$ using the Luminous Red Galaxies (LRGs) sample from the extended Baryon Oscillation Spectroscopic Survey (eBOSS; Dawson et al. 2016).

The paper is organized as follows: Section 2 presents the data, Section 3 describes the mock catalogs used for the estimation of the covariance matrix and for our systematics checks. Section 4 presents the modeling of the RSD signal as well as the parametrization used for the Alcock-Paczynski test. Section 5 describes the methodology followed in our analysis. Section 6 presents our analysis, using mock catalogs, of the systematic effects associated with our methodology. The results for the eBOSS-CMASS sample are presented in Section 7. Finally, the cosmological implications of this work are reviewed in Section 8.

2 DATA

Our sample of spectroscopic data was collected during the first two years of eBOSS (Dawson et al. 2016), which is the cosmological component of the fourth generation of the Sloan Digital Sky Survey (SDSS-IV; Blanton et al. 2017). All of our spectra were obtained by the Sloan 2.5m telescope using two multi-object spectrographs (Smee et al. 2013) at Apache Point Observatory in New Mexico, USA (Gunn et al. 2006). All of these data belong to the SDSS Data Release 14 (Abolfathi et al. 2017), of which we analyze the Luminous Red Galaxies (LRG) Sample. The LRG targets were selected based on updated photometric data from SDSS I/II/III imaging (Fukugita et al. 1996; Gunn et al. 1998) for which the calibration of the photometric data was updated following the procedure presented in Schlafly & Finkbeiner (2011). The target selection process also used infrared photometry data from the Wide-Field Infrared Survey Explorer (WISE; Wright et al. 2010). The WISE satellite observed the entire sky using four infrared channels respectively centered at $3.4 \mu\text{m}$ (W1), $4.6 \mu\text{m}$ (W2), $12 \mu\text{m}$ (W3), and $22 \mu\text{m}$ (W4). The eBOSS LRG sample uses the W1 and W2 bands. Given that stars have different properties than galaxies in infrared (particularly due to the galactic dust), the WISE data allow us to reduce the stellar contamination, it is also useful for extending the redshift range with respect to BOSS. The target selection follows the algorithm described in Prakash et al. (2016).

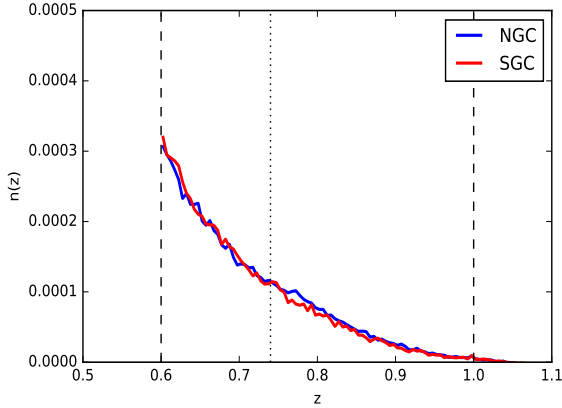


Figure 1. Number density of the LRG sample as a function of the redshift (solid lines) for both hemispheres, in blue for the North Galactic Cap (NGC) and in red for the South Galactic Cap (SGC); the dashed vertical lines indicate the redshift cuts applied. The median redshift of the sample is $z = 0.72$ and is represented by the vertical dotted line.

2.1 eBOSS-CMASS Sample

Our eBOSS DR14 LRG Sample includes data of the first two years of the eBOSS program combined with the BOSS CMASS data (Alam et al. 2017a) which overlaps with the eBOSS footprint in a redshift range of $0.6 < z < 1.0$. This approach allows construction of a more complete sample without decreasing the median redshift.

The eBOSS-CMASS sample is composed of 80118 galaxies from eBOSS and 46439 from CMASS, yielding a total of 126,557 galaxies. The numbers separated by Galactic hemisphere are listed in table 1. The sky coverage in the North Galactic Cap (hereafter NGC) is 1011.15 deg^2 and 788.09 deg^2 in the South Galactic Cap (hereafter SGC), giving a total solid angle of 1844.0 deg^2 . The effective volume of eBOSS is 0.618 Gpc^3 which increases up to 0.9 Gpc^3 when considering the eBOSS-CMASS sample.

Figure 1 shows the number density of the sample as a function of redshift (solid lines) for both hemispheres, in blue for the NGC and in red for the SGC; the dashed vertical lines indicate the redshift cuts applied for our analysis. The median redshift of the sample is $z = 0.72$, which is represented by the vertical dotted line.

2.2 Footprint and Masks

The left and right panels of Figure 2 display the sky coverage of the galaxy sample for the NGC and SGC respectively, where the color scale indicates the targeting completeness defined as:

$$C = \frac{N_{\text{gal}} + N_{\text{qso}} + N_{\text{star}} + N_{\text{cp}} + N_{\text{zfail}}}{N_{\text{target}}}, \quad (2)$$

where

- N_{gal} is the number of galaxies with good quality eBOSS spectra.
- N_{cp} is the number of galaxies without spectra due to the fiber collision effect. Two fibers cannot be closer than $62''$ on a given plate.

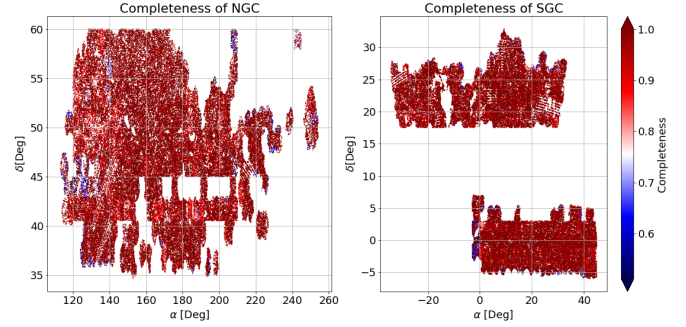


Figure 2. Angular mask of the North Galactic Cap NGC (left) and the South Galactic Cap SGC (right). The color indicates the targeting completeness of the DR14 LRG sample in a given area of the sky, which is computed using equation 2. Regions of low targeting completeness (where $C < 0.5$) were not included in the final sample.

- N_{star} denotes the number of observed objects which are spectroscopically confirmed to be stars.
- N_{zfail} denotes the number of objects for whom the measured spectra lacks sufficient qualities to provide a confident redshift measurement.

The targeting completeness is computed by sector, and the mean completeness is 96.3% (where the NGC has an average completeness of 95.9% and the SGC 96.9%). We only use data from regions with a completeness higher than 0.5 (this value is smaller than the completeness used in BOSS).

Certain areas in the sky have to be excluded from the final data sample. The maps of these excluded regions are known as veto masks. These regions have to be removed from our random catalogs as well. The veto masks used in eBOSS were:

- The Collision priority veto mask that excludes regions that are closer than $62''$ from an already observed target, as any object inside this radius would not be observed due to fiber collision.
- The Bright veto mask which excludes regions around stars that are part of the Tycho catalog (Høg et al. 2000) with Tycho BT magnitudes larger than 6 and lower than 11.5. The excluded radius is magnitude-dependent and it goes from $0.8'$ to $3.4'$. An additional mask excludes regions around bright galaxies and other objects (Rykoff et al. 2014); it is also magnitude-dependent and goes from a radius of $0.1'$ to $1.5'$.
- The Bad fields veto mask excludes regions of the sky with bad photometry. If the local sky is badly determined (as occasionally happens in regions with complex backgrounds), the core of an object can be strongly negative.
- The Extinction Mask excludes regions where the Galactic extinction is such that $E(B - V) > 0.15$ or where the seeing FWHM is larger than $2.3''$, $2.1''$, and $2.0''$ in g , r , and i bands, respectively.
- The Center Focal Plane Mask excludes LRG targets that lie within $92''$ of the center of the telescope focal plane, where a center post holds the plate and prevents fibers from being assigned.

Table 1. Characteristics of the LRG data catalogs used. The left panel corresponds to the BOSS CMASS sample from DR12, the right to the eBOSS LRG DR14 sample. N_{star} and N_{qso} are the number of objects whose spectra were determined to be stars or quasars instead of LRGs. N_{zfail} is the number of objects whose redshift measurement was not reliable, and N_{cp} the number of objects without spectra due to close pair effects. The last line reports the number of galaxies and the effective volume of our final sample, which is a combination of the CMASS and eBOSS samples.

CMASS LRG Sample DR12							
Catalogue	Area (deg ²)	Total redshifts					
CMASS-BOSS NGC	1011.15	26149	-	-	-	-	-
CMASS-BOSS SGC	788.09	20290	-	-	-	-	-
eBOSS LRG DR14 Sample							
Catalogue	N_{gal}	N_{star}	N_{qso}	N_{cp}	N_{zfail}	$A_{\text{eff}}[\text{deg}^2]$	$V_{\text{eff}}[\text{Gpc}^3]$
eBOSS NGC	45826	2897	18	2263	4957	1033.4	0.356
eBOSS SGC	34292	4273	18	1687	4366	811.6	0.262
Total	80118	7170	36	3950	9323	1844.0	0.618
eBOSS-CMASS	126557						0.900

The total masked area is 12.3% for the NGC and 18.2% for the SGC.

2.3 Catalogue for LSS analysis

Two data catalogs that differ in their treatment of the photometric systematics and of spectroscopic incompleteness were used to create the sample for our study. The first is a BOSS-like catalog where traditional weighting schemes are applied, described in [Ross et al. \(2017\)](#), to the data. The second is denoted as the "official catalog", and it was used in [Bautista et al. \(2017\)](#) for performing the BAO analysis. Here some improvements with respect to previous analysis were implemented: the forward modeling of the randoms for the spectroscopic incompleteness and the multilinear regression and subsampling of the randoms for the photometric systematics.

In this section, we briefly review both methodologies, first describing the different treatments of the photometric systematics, and then the procedures used for dealing with the redshift incompleteness. Finally, we summarize the weights applied to the data for both cases and also the subsampling techniques used in the random catalogs in each case.

2.3.1 Correcting for Photometric Systematics

Here we will give a brief description of the two methodologies for correcting photometric systematics:

- Iterative method ("BOSS-like") was developed in [Ross et al. \(2017\)](#). The basic idea is to include the systematics in an iterative way and estimate at each step the associated weights. For the eBOSS LRG sample, we studied the correlation of the mean density as a function of seven potential observational systematics related with SDSS photometry: stellar density, i -band depth, z -band sky flux, z -FWHM, and r -band extinction¹. We followed the iterative method starting with the main systematics reported in previous works.

¹ Additionally we explored two additional maps derived from WISE photometry: one for the median number of single-exposure frames per pixel in the WISE W1 band (denoted as WISE W1 Cov Med) and the median of accumulated flux per pixel in the WISE W1 band (denoted by WISE W1 Med).

Figure 3 displays the mean density of data, N_{gal} , normalized by the random number density, N_{ran} , as a function of six of the seven systematics considered in the analysis before and after corrections. The most significant weights are those due to stellar density (w_{star}), followed by the r -band extinction (w_{ext}), airmass (w_{air}), and z -band sky flux (w_{sky}). The systematics related with the WISE maps did not have any strong correlation requiring correction, thus we decided not to include them in the weight estimation. We calculate a weight for each galaxy that takes in account a linear relationship for each potential systematic.

$$w(\text{sys}) = \frac{1}{mx + b}. \quad (3)$$

The total systematic weight $w_{\text{sys tot}}$, is defined as

$$w_{\text{SYSTOT}} = w_{\text{star}} w_{\text{ext}} w_{\text{air}} w_{\text{sky}} \quad (4)$$

- Multi-regression Method: We followed the same methodology presented in [Bautista et al. \(2017\)](#), where the correlation between systematic maps and density were computed using a multilinear regression of the seven systematic maps instead of the iterative method. The advantage of this method is that it does not assume the systematics are independent, as does the iterative method. Additionally, in the official catalogs, instead of using weights associated with galaxies, the randoms are subsampled following the correlation found with the multi-regression method; the subsampling of the randoms or the weighting scheme of the galaxies should yield the same results; the main differences observed in the catalogs should be derived uniquely from the Iterative/Multi-regression methodologies.

Figure 4 presents the multipoles for the eBOSS sample (NGC and SGC separated), comparing the iterative and multilinear regression methods. The monopole from both hemispheres without corrections shows a large spurious correlation at large scales that is reduced when either of the methods for correcting the observational systematics is applied. There is an excellent agreement in both methods for correcting photometric systematics. The SGC does show slightly better performance using the multi-regression method.

2.3.2 Correcting for Spectroscopic Completeness

Previous analyses on the eBOSS LRG sample reported that fluctuations in the (S/N) significantly affect the probability

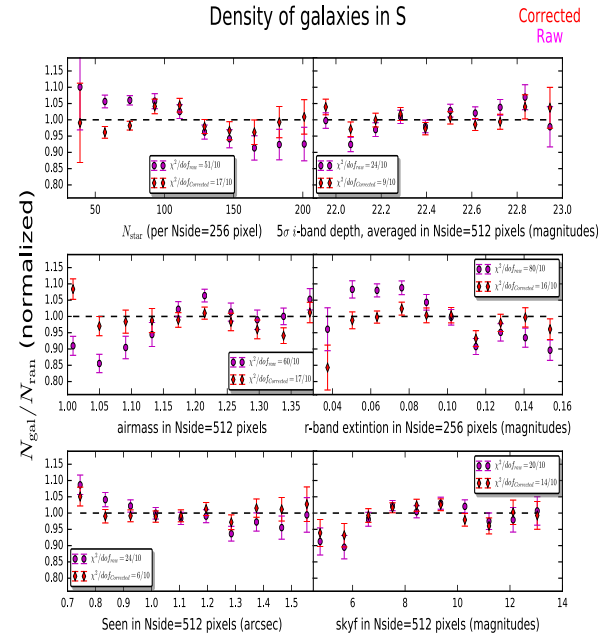
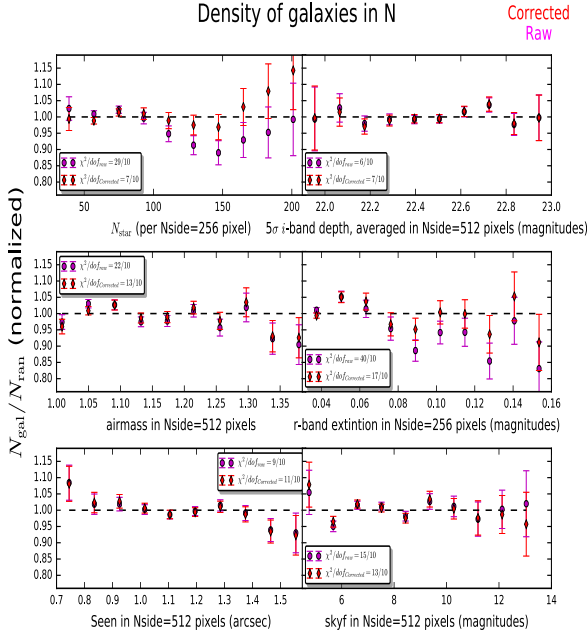


Figure 3. We show the mean density of data, N_{gal} , normalized by the random number density, N_{rand} as a function of six of the nine systematics considered in the analysis. The most significant weights were those due to stellar density (w_{star}), r-band extinction (w_{ext}), airmass (w_{air}), and z-band sky flux (w_{sky}).

of obtaining a confident redshift (See Figure 5 of Bautista et al. 2017). Additionally, the probability of obtaining a confident redshift varies across the focal plane, decreasing near the edges (See Figure 6 of Bautista et al. 2017). We define the failure rate as:

$$\eta = \frac{N_{\text{gal}}}{N_{\text{zfail}} + N_{\text{gal}}} \quad (5)$$

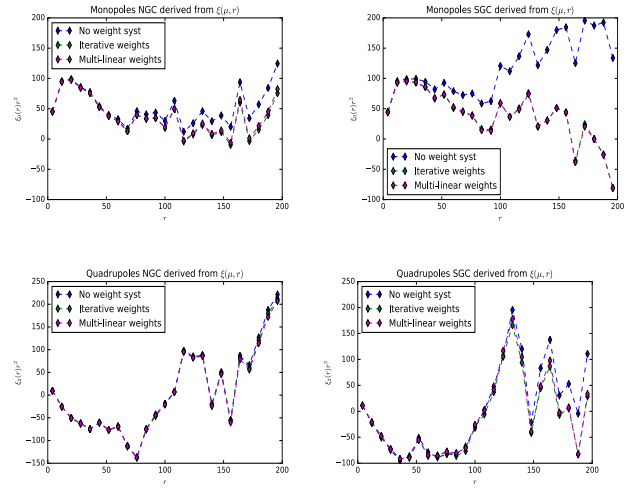


Figure 4. Multipoles for eBOSS sample (NGC left and SGC right) comparing the iterative and multilinear regression methods. The monopole from both hemispheres without corrections shows a large spurious correlation at large scales in monopole that is reduced when either of the methods for correcting the observational systematics is applied.

where N_{gal} is the number of usable galaxies and N_{zfail} the number of rejected galaxies due to the redshift failure. The failure rate in eBOSS LRGs is 10%, which is significantly higher than previous surveys; for example, in BOSS the failure rate was only 1.8% (This is due to eBOSS targeting fainter galaxies than BOSS).

The variations of the failure rate across the focal plane could bias the clustering measurements. In order to account for the effect of this redshift incompleteness, we applied two methods to mitigate the effect on the clustering measurements; in particular, we studied how the two techniques affect the RSD analysis.

- **Nearest-neighbor up-weighting.** The procedure followed in BOSS (Reid et al. 2012) was to upweight the nearest neighbor with a good redshift and spectroscopic classification in its target class, within a sector. It has been shown that this method introduces structure into the monopole at small scales, and also modifies the quadrupole amplitude, which could potentially affect the growth factor measurements.

- **Forward-Modeling.** This approach uses a probabilistic model that depends on the position of its fiber in the focal plane and the overall signal-to-noise ratio of the plate. The model for failures is then applied to the random sample by subsampling, mimicking the patterns retrieved in the model. For more details about this modeling we refer the reader to Bautista et al. (2017).

2.3.3 Data Weights

We now specify the weights applied for each catalog and the randoms treatment.

- **w_{SYSTOT} .** As described previously, these weights account for the fluctuations of the observational conditions that can impact the clustering signal. For the BOSS-like method

these weights are computed as described in the Iterative Method. For the official catalogs these weights are set to 1, as the photometric systematics are taken into account in the randoms by using subsampling techniques.

- w_{FKP} . These weights are used for both set of catalogs. They serve to optimize clustering signal-to-noise ratio for a survey with density varying with respect to the redshift. Also known as FKP weights (Feldman et al. 1994), they are defined as:

$$w_{\text{FKP}} = \frac{1}{1 + \bar{n}(z)P_0}, \quad (6)$$

where $\bar{n}(z)$ is the average comoving density of galaxies as a function of redshift and P_0 is the value of the power spectrum at scales relevant for our study ($k = 0.14h.\text{Mpc}^{-1}$). For the eBOSS LRG sample we adopt a value of $P_0 = 10^4 h^{-3}.\text{Mpc}^3$, which is the same value used in the final BOSS CMASS clustering measurements.

- w_{CP} . This weight accounts for the fiber collisions and is used for both catalogs. Targets missed due to fiber collisions do not happen randomly on the sky; they are more likely to occur in overdense regions. For mitigating this effect we followed the up-weighting technique described previously.

- w_{NOZ} . This weight accounts for the redshift failures. For the BOSS-like method this weight is computed for each galaxy following the up-weighting technique described in the previous section. For the official catalogs these weights are set to 1, as the spectroscopic incompleteness is modeled to subsample the randoms as described in the previous section.

3 MOCKS

We use three different sets of mock catalogs in our analysis. The first is a collection of 1000 Quick Particle Mesh (QPM) mocks (White et al. 2014), which will be used for computing the covariance matrices and for doing several systematic tests. The second one is a set of 1000 Effective Zeldovich approximation method (EZ) mocks (Chuang et al. 2015), that are used to test variance of our fitting methodology. The third catalog is a set of 84 high-fidelity mocks called CutSky-Mocks Alam et al. (2017a). These catalogs will be necessary for testing the accuracy of the model used.

3.1 QPM Mock Catalogs

The QPM method is described in White et al. (2014). QPM mocks use low-resolution PM simulations to model the density field at each time step. A Halo Occupation Distribution (HOD) framework is adopted for populating halos with galaxies following the 5-parameter method described in Tinker et al. (2012) where satellite galaxies are distributed inside halos following a Navarro-Frenk-White profile. The HOD parameters were tuned to the DR14 eBOSS LRG sample in Zhai et al. (2017).

The cosmology used to compute these mocks is $\Omega_{\text{M}} = 0.29$, $h = 0.7$, and $\Omega_{\text{b}}h^2 = 0.02247$. The same boxes were used for generating NGC and SGC mocks, thus there should be a small correlation between them (particularly in the large modes). In order to mitigate this effect, we combined mocks produced by different realizations of the NGC and the SGC. The mask that we applied to the mocks will be described in

Section 2.2. We will use two sets of 1000 realizations, one for the NGC and another for the SGC. Also, our random catalogs have a density $50 \times$ larger than the data density; this procedure was adopted in order to reduce their statistical noise contributions to the two-point correlations estimator.

Our QPM mocks are needed for two reasons: to compute an estimate of the covariance matrix and to test our methodology. Figure 5 shows the mean of the mocks compared with the data; the solid lines represent the mean of the mocks correlation function and the dotted lines the data correlation function multipoles. There is a good agreement between the data and the mocks for scales larger than $30 h^{-1}\text{Mpc}$; at smaller radii a mismatch appears, which might be related to the resolution of the mocks.

3.2 EZ Mock Catalogs

EZ simulations are light-cone mock catalogs created following the Effective Zeldovich methodology described in Chuang et al. (2015). In order to construct the eBOSS+CMASS sample, the CMASS and eBOSS mocks are calibrated and generated separately and then combined. The CMASS mocks are constructed in four redshift bins: (0.55, 0.65), (0.65, 0.7), (0.7, 0.8), and (0.8, 1.0025), while the eBOSS mocks are constructed at five redshift bins: (0.55, 0.65), (0.65, 0.7), (0.7, 0.8), (0.8, 0.9), and (0.9, 1.05). The fiducial cosmology is a flat ΛCDM model with $\Omega_{\text{M}} = 0.307115$, $h = 0.6777$, $\sigma_8 = 0.8225$, $\Omega_{\text{b}} = 0.048206$ and $n_{\text{s}} = 0.9611$. We will use these mocks to test the variance of the fitting methodology.

3.3 N-Series Cut Sky Mocks

Our N-Series Cut Sky Mock library contains 84 mocks generated with N-body simulations that were done using GADGET2 (Springel 2005). Our mocks have the angular and radial mask of BOSS NGC DR12. We used this mock catalog to test the theoretical systematics related to our modeling methodology. The N-Series cosmology is $\Omega_{\text{M}} = 0.286$, $h = 0.7$, $\Omega_{\text{b}} = 0.047$, $\sigma_8 = 0.820$, and $n_{\text{s}} = 0.96$.

4 MODELING REDSHIFT SPACE DISTORTIONS

In order to model the different multipoles of the two-point correlation function, we use the combined Convolutional Lagrangian Perturbation Theory (CLPT) and Gaussian Streaming RSD (CLPT-GSRSD) formalism, developed by Wang et al. (2014), Reid & White (2011a), and Carlson et al. (2013). In this section we briefly describe this theoretical framework.

4.1 CLPT

CLPT provides a non-perturbative resummation of Lagrangian perturbation to the two-point statistic in real space for biased tracers. The starting point for the Lagrangian

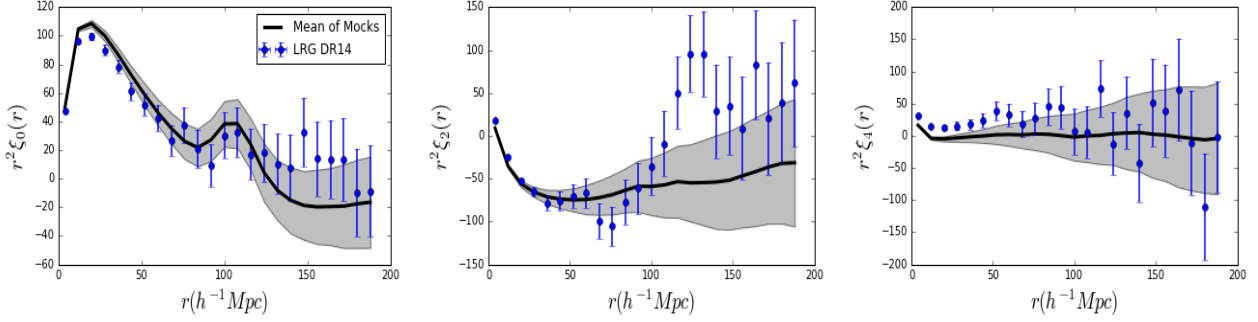


Figure 5. The Black solid lines are the mean of our 1000 QPM mocks for the Monopole (left), Quadrupole (center), and Hexadecapole (right); the shaded regions are the $1\text{-}\sigma$ variations. The blue dots represent the data points and the associated error bars and are equal to the $1\text{-}\sigma$ variation shown in the shaded contours.

framework is the relation between the Lagrangian coordinates \vec{q} that are related to the Eulerian coordinates \vec{x} as:

$$\vec{x}(\vec{q}, t) = \vec{q} + \vec{\Psi}(\vec{q}, t), \quad (7)$$

where $\Psi(\vec{q}, t)$ is the displacement field at each time t . The two-point correlation function is expanded in its Lagrangian coordinates considering the tracer X , in our case the Luminous Red Galaxies, to be locally biased with respect to the initially Cold Dark Matter overdensity $\delta(\vec{q})$. The expansion is performed over different orders of the Lagrangian bias function $F[\delta(\vec{q})]$, defined as:

$$1 + \delta_X(\vec{q}, t) = F[\delta(\vec{q})]. \quad (8)$$

The Eulerian contrast density field is computed convolving with the displacements:

$$1 + \delta_X(\vec{x}) = \int d^3q F[\delta(\vec{q})] \int \frac{d^3k}{(2\pi)^3} e^{i\vec{k}(\vec{x} - \vec{q} - \vec{\Psi}(\vec{q}))}. \quad (9)$$

Assuming that the expectation value of the n^{th} derivative of the Lagrangian bias function F is given by:

$$\langle F^n \rangle = \int \frac{d\delta}{\sqrt{2\pi}\sigma} e^{-\delta^2/2\sigma^2} \frac{d^n F}{d\delta^n}, \quad (10)$$

the two-point correlation function is obtained by evaluating the expression $\xi_X(\vec{r}) = \langle \delta_X(\vec{x}) \delta_X(\vec{x} + \vec{r}) \rangle$ corresponding to Eq 19 of [Carlson et al. \(2013\)](#) and which can be simplified using the bias expansion as in their Eq. 43:

$$1 + \xi_X(\vec{r}) = \int d^3q M(\vec{r}, \vec{q}), \quad (11)$$

where $M(\vec{r}, \vec{q})$ is the kernel of convolution taking into account the displacements and bias expansion up to its second derivative term. The bias derivative terms are computed using a linear power spectrum (LPS). The LPS that we used was computed using the code CAMB ([Lewis et al. 2000](#)) for a fixed cosmology described as the fiducial cosmology of our analysis.

As we are interested in studying RSD, we also must model the peculiar velocity's effect on the clustering statistic. CLPT can compute the pairwise velocity distribution \vec{v}_{12} and the pairwise velocity dispersion σ_{12} . This calculation is done following the formalism of [Wang et al. \(2014\)](#) which is

similar to the one describe above but modifying the kernel to take into account the velocities rather than the density:

$$\vec{v}_{12}(r) = (1 + \xi(\vec{r}))^{-1} \int M_1(\vec{r}, \vec{q}) d^3q, \quad (12)$$

and

$$\sigma_{12}(r) = (1 + \xi(\vec{r}))^{-1} \int M_2(\vec{r}, \vec{q}) d^3q. \quad (13)$$

The kernels $M_{1,2}(\vec{r}, \vec{q})$ also depend on the first two derivatives of the Lagrangian bias $\langle F' \rangle$ and $\langle F'' \rangle$, which are free parameters, in addition to the growth factor f , for our model. Hereafter we eliminate the brackets for the Lagrangian bias terms to have a less cumbersome notation in the following sections.

4.2 CLPT-GSRSD

While CLPT generates more accurate multipoles than the Lagrangian Resummation Theory (LRT) from [Matsubara \(2008\)](#) and the linear theory, we still require better performance to study the smaller scales of our quadrupoles. This represents an issue that is particularly important when doing RSD measurements as the peculiar velocities are generated by interactions that occur on the scales of clusters of galaxies.

In order to achieve the required precision, we map the real space CLPT models of the two-point statistics into redshift space following the Gaussian Streaming Model (GSM). This formalism was proposed by [Reid & White \(2011b\)](#). Here, the pairwise velocity distribution of tracers is assumed to have a Gaussian distribution that is dependent on both the separation of tracers r and the angle between their separation vector and the line-of-sight μ .

The methodology of using CLPT to model the necessary inputs of a GSM was implemented by [Wang et al. \(2014\)](#). Its predictions are computed via the following integral:

$$1 + \xi(r_{\perp}, r_{\parallel}) = \int \frac{1}{\sqrt{2\pi(\sigma_{12}^2(r, \mu) + \sigma_{\text{FoG}}^2)}} [1 + \xi(r)] \times \exp - \frac{[r_{\parallel} - y - \mu v_{12}(r, \mu)]^2}{2(\sigma_{12}^2(r, \mu) + \sigma_{\text{FoG}}^2)} dy, \quad (14)$$

where, as stated, $\xi(r)$, $v_{12}(r)$, and $\sigma_{12}(r)$ are computed from CLPT.

Reid & White (2011b) demonstrated that GSM can predict accuracies of $\approx 2\%$ when DM halos are used as tracers. However, not all LRGs are central halo galaxies; approximately 20% of them are satellite galaxies with a peculiar velocity respect to their host halo. Therefore, we need to consider a contribution to the velocity dispersion due to the *Fingers of God* (FoG) effects on non-linear scales. We have addressed this point by adding the σ_{FoG} parameter to Eq. 14.

To summarize, given a fiducial cosmology, our model has four free parameters $[f, F', F'', \sigma_{\text{FoG}}]$. The cosmology determines the LPS used in the model. The following subsection describes how we include variations of the cosmological parameters around the fiducial values using the Alcock-Paczynski Test.

4.3 Including the Alcock-Paczynski Effect

We described above the model for the RSD signal given a fixed fiducial cosmology that determines the LPS to be used. However, we can extract additional information by measuring the galaxy clustering along the line-of-sight and perpendicular to the line-of-sight, and we can extract geometrical information via the Alcock-Paczynski (AP) test (Alcock & Paczynski 1979). The AP test describes a distortion in an otherwise isotropic feature in the galaxy clustering when the assumed fiducial cosmological model used to transfer the measured redshifts into distances deviates from the true cosmology. In this work, for extracting AP information, we use the parametrization described in Xu et al. (2012), Vargas-Magaña et al. (2014), and Anderson et al. (2014), which derives measurements of the isotropic dilation of the coordinates parametrized by α and the anisotropic warping of the coordinates parametrized by ϵ . Here α and ϵ parametrize the geometrical distortion derived from assuming an incorrect cosmology when calculating the galaxy correlation function. The parameters α and ϵ are defined as:

$$\alpha = \alpha_{\perp}^{2/3} \alpha_{\parallel}^{1/3}, \quad 1 + \epsilon = \left(\frac{\alpha_{\parallel}}{\alpha_{\perp}} \right)^{1/3}. \quad (15)$$

where α_{\perp} and α_{\parallel} are defined in terms of dilation in the transverse and line-of-sight directions, given by a difference between the fiducial cosmology and the “true cosmology”.²

The parameters α and ϵ are related to $D_A(z)/r_s$ and $cz/(H(z)r_s)$, where $D_A(z)$ is the angular diameter distance to redshift z , r_s is the sound horizon at radiation drag, and $H(z)$ is the Hubble parameter. Finally, α_{\perp} and α_{\parallel} are related to $D_A(z)/r_s$ and $cz/(H(z)r_s)$ via:

$$\alpha_{\perp} = \frac{D_A(z)r_s^{\text{fid}}}{D_A^{\text{fid}}r_s}, \quad (16)$$

and

$$\alpha_{\parallel} = \frac{H^{\text{fid}}(z)r_s^{\text{fid}}}{H(z)r_s}. \quad (17)$$

² Note that $\alpha = 1$ and $\epsilon = 0$ for the mocks, if we use their natural cosmology as the fiducial cosmology for the analysis.

Table 2. Expected values of cosmological parameters for the QPM mocks and Fiducial Cosmology at different redshift ranges/model. The units for $H(z)$ are $\text{km s}^{-1}\text{Mpc}^{-1}$ and (Mpc) for $D_A(z)$.

Model	z-range	z_{eff}	$f(z)$	$\sigma_8(z)$	$f(z)\sigma_8(z)$	$H(z)$	$D_A(z)$
QPM	[0.6, 1.0]	0.72	0.806	0.557	0.449	-	-
Fiducial	[0.6, 1.0]	0.72	0.819	0.550	0.450	101.94	1535
Nseries	[0.43, 0.7]	0.5	0.740	0.637	0.471	-	-

5 METHODOLOGY

5.1 Fiducial Cosmology

Our analysis is performed using the following fiducial cosmology:

$$\begin{aligned} \Omega_M &= 0.31, \\ \Omega_{\Lambda} &= 0.69, \\ \Omega_k &= 0, \\ \Omega_b h^2 &= 0.022, \\ \Omega_c h^2 &= 0.00064, \\ w &= -1, \\ w_a &= 0, \\ h &= 0.676, \\ n_s &= 0.97, \\ \sigma_8 &= 0.8. \end{aligned}$$

This fiducial cosmology is different from the ones used to compute the mocks; this additional bias in our methodology has to be considered. This extra bias will be defined in Section 6.

5.2 2PCF Estimator

As stated earlier, we need to compute the two-point clustering statistics of the DR14 LRG sample described in Section 2 and compare our results to predictions of the CLPT-GSRSD model described in 4. We are interested in constraining RSD parameters. Therefore, we must study the clustering of galaxies in two directions: the one parallel to the LOS, where peculiar velocities of infalling galaxies generate RSD, and its perpendicular direction, where no distortion occurs. We decompose the vector \vec{r} , which represents the distance between two galaxies, into two components: r_{\parallel} parallel to the LOS and r_{\perp} that is perpendicular to it:

$$r^2 = r_{\parallel}^2 + r_{\perp}^2. \quad (18)$$

While this approach is an intuitive parametrization for investigating RSD, we will be using a different, but equivalent one. Let θ denote the angle between the galaxy pair separation and the LOS direction, and let μ be defined as $\mu = \cos \theta$. We then have the relation:

$$\mu^2 = \cos^2 \theta = \frac{r_{\parallel}^2}{r^2}, \quad (19)$$

and our two direction parameters will be $[r, \mu]$.

The 2D-correlation function $\xi(r, \mu)$ is computed using the Landy-Szalay estimator (Landy & Szalay 1993):

$$\xi(r, \mu) = \frac{DD(r, \mu) - 2DR(r, \mu) + RR(r, \mu)}{RR(r, \mu)}, \quad (20)$$

where $DD(r, \mu)$, $RR(r, \mu)$, and $DR(r, \mu)$ are the number of pairs of galaxies which are separated by a radial separation r and angular separation μ . The three symbols represent the data-data, random-random, and data-random pairs, respectively.

The multipoles are Legendre moments of the 2D-correlation function $\xi(r, \mu)$, and can be computed using the following equation:

$$\xi_\ell(r) = \frac{2\ell + 1}{2} \int_{-1}^{+1} d\mu \xi(r, \mu) L_\ell(\mu), \quad (21)$$

where $L_\ell(\mu)$ is the ℓ -th order Legendre polynomial.

We will focus primarily on the monopole, the quadrupole, and the hexadecapole ($\ell = 0$, $\ell = 2$, and $\ell = 4$).

The pair-counts were computed using the public code CUTE (Alonso 2012). However, there are three corrections to be considered when using the LS equation (20):

- The number of galaxies in the Data catalogs (N_D) is approximately 50 times smaller than the ones in our random catalogs (N_R). Therefore the Random and Data pairs should be compared as

$$\frac{DD(r, \mu)}{RR(r, \mu)} \times \frac{N_R(N_R - 1)}{2} \times \frac{2}{N_D(N_D - 1)}.$$

- The number of galaxies in the SGC ($N_{D,S}$) is smaller than those in the NGC ($N_{D,N}$). Therefore the total number of pairs should be added as:

$$DD(r, \mu) = \frac{2(DD_N(r, \mu) + DD_S(r, \mu))}{(N_{D,N}(N_{D,N} - 1) + N_{D,S}(N_{D,S} - 1))}.$$

- Each galaxy has a particular weight w_i as described in Section 2. Hence, the total number of galaxies in any catalog is weighted as

$$N^w = \sum w_i.$$

5.3 Fitting

Unless stated otherwise, we will be using 13 bins of $8h^{-1}\text{Mpc}$ in width, in the interval between $[28h^{-1}\text{Mpc}, 124h^{-1}\text{Mpc}]$. Given that we will be working with either the first two non-zero multipoles or the first three (depending on the test), the analysis will have a total of either 26 or 39 bins.

The next step is to compare our measured two-point statistics with those predicted by our model. In particular, we want to find the values of our free parameters that correspond to the model that is closer to the measured two-point correlation function.

In order to find identify best-fit parameters, we minimize the χ^2 function,

$$\chi^2 = (\vec{m} - \vec{d})^T C^{-1} (\vec{m} - \vec{d}) \quad (22)$$

where \vec{m} is the vector formed by the model predictions, and \vec{d} is the equivalent vector observed from our data. Examining Eq. 22 reveals that the smaller the value of χ^2 , the more similar \vec{m} is to \vec{d} .

The sample covariance is defined as:

$$C_{ij} = \sum_{m=1}^{N_{\text{mocks}}} (\xi_i^m - \bar{\xi}_i)(\xi_j^m - \bar{\xi}_j), \quad (23)$$

where N_{mocks} is the number of mocks, and $\bar{\xi}_i$ is the average of the i^{th} bin.

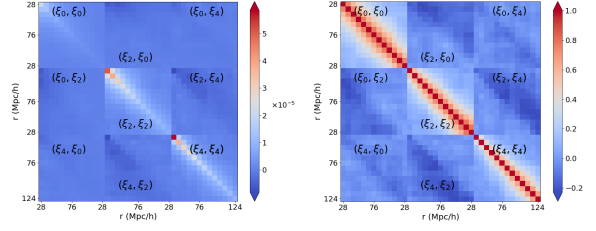


Figure 6. Density map of the Covariance matrix (left) computed from our 1000 QPM Mocks simulations. The matrix has 13 bins in r and 3 multipoles. The right panel presents the correlation matrix defined as $\text{Corr}_{ij} = \frac{C_{ij}}{\sqrt{C_{ii}C_{jj}}}$. The normalization is done such that the diagonal is always unity, and it shows how much covariance (off-diagonal) there is compared to our variance (diagonal).

We scale the inverse sample covariance matrix, C_s^{-1} , using Eq. 17 of Hartlap et al. (2007):

$$C^{-1} = C_s^{-1} \frac{N_{\text{mocks}} - N_{\text{bins}} - 2}{N_{\text{mocks}} - 1}. \quad (24)$$

This procedure corrects for the fact that the matrix in Eq. 23 is a biased estimate of the true inverse covariance matrix C^{-1} .

Figure 6 shows the covariance and correlation matrix computed from 1000 QPM mocks. Most of our error arises from the elements on the diagonal (variance of a given bin), but there is also a significant contribution coming from elements outside of the diagonal (covariance between different bins).

6 TESTING FOR SYSTEMATIC UNCERTAINTIES

6.1 Testing Accuracy of GSRSD Hexadecapole Model with High-Resolution Simulations

This section is dedicated to testing the performance of the methodology developed in Section 5. Here, we will use the N-Series CutSky mocks described in Section 3 to check the reliability of the CLPT model with regards to recovering the cosmological parameters. These are high resolution mocks built with the BOSS-CMASS properties that allow us to study the accuracy of the model. We will run our fitting methodology on these high-fidelity mocks in order to test if their fiducial parameters can be recovered. The N-Series CutSky mocks have been used previously in the literature for testing the monopole- and quadrupole-only methodologies.

We fit our N-series CutSky mocks twice, the first using only the monopole and the quadrupole, and the second including the hexadecapole. The sample covariance matrix used to perform these fits is computed using the QPM-BOSS CMASS sample re-scaled to match the mocks volume, and provides our error estimate (the covariance matrix obtained from N-Series would be quite noisy given the limited number of realizations available). The pair-counts of our mocks were computed using the mocks cosmology to transform angular positions and redshifts into comoving coordinates. To be consistent, the CLPT-GSRSD input template was also computed using the cosmology of the mocks.

The expected values of the linear growth rate of f (f_{exp}) are reported in Table 2 for the natural cosmology of the mocks. We define the bias of the growth factor estimation b_f as:

$$b_f = \langle f_{\text{measured}} \rangle - f_{\text{exp}} \quad (25)$$

We use the measurement of the Eulerian bias $b = 2.3$ performed by Zhai et al. (2017) as reference. This estimate was computed using our same sample with the addition of an HOD model.

The left panel of Figure 7 shows the mean of the multipoles; the error bars are the diagonal terms of the covariance matrix divided by $1/\sqrt{N_{\text{Mock}}}$. The different colors represent the best fit model for the mean of the mocks at different minimum scales of the fits when the cuts are applied to all multipoles.

The model using the hexadecapole fitted at the full range (blue lines) does not match the mean of the mocks accurately for quadrupole and hexadecapole as shown in the residuals. Increasing the minimum range of the fit affects mostly the quadrupole at large scales and has little effect on the monopole and hexadecapole and does not improve the match of hexadecapole at large scales. By comparing the residual plots of the green and blue lines we can tell that it is not clear which range fits the quadrupole and hexadecapole better, the full range appears to overestimate the large scales and cutting the scales tends to underestimate.

The right panel of Figure 7 displays an exercise similar to the one in the left panel, except this time we only adopt a higher value for the minimum scale of the hexadecapole, in this case the effects of varying the minimum scale of the fits are reduced also for the quadrupole. The model considering the hexadecapole cutting the small scales match slightly better the multipoles but do not improve significantly compared with the model using the hexadecapole in the full range or considering only the monopole and quadrupole.

Table 3 reveals that a smaller bias is obtained when using the full range $[27.5-127.5] h^{-1}\text{Mpc}$ of the hexadecapole ($b_f < 0.001$, compared with the value of $b_f = 0.052$ obtained when all multipoles are in the range $[47.5-127.5] h^{-1}\text{Mpc}$). However, when we include the hexadecapole the best values of the $\chi^2/\text{d.o.f}$ is obtained when using the range between $[47.5-127.5] h^{-1}\text{Mpc}$ for all multipoles (i.e. $\chi^2/\text{d.o.f} = 102/45 = 2.1$).

Let us compare the results including the hexadecapole to those where only the monopole and the quadrupole were used. The fit with the smallest $\chi^2/\text{d.o.f}$ (0.92) is obtained for the monopole and quadrupole only fits, where the bias has a value of $b_f = 0.014$. When we fit the three multipoles and constrain the hexadecapole range, we find $\chi^2/\text{d.o.f} = 244/57 = 4.3$ and the bias is $b_f < 0.001$. The right panel of Figure 7 demonstrates that the best fit model for both cases is very similar. A closer inspection of the rest of the parameters indicates that the best-fit parameters for α and ϵ are slightly more biased when we use the hexadecapole, where the biases are $|b_\alpha| = |b_\epsilon| = 0.003$, compared to $|b_\alpha| = |b_\epsilon| = 0.001$ when using only monopole and quadrupole. Finally, the results are globally better using only the monopole and the quadrupole, especially considering the reduced χ^2 values. However, given that Zarrouk et al. (2018) successfully included the hexadecapole in their RSD analysis on the QSO sample, we will explore the study

of the hexadecapole's impact on the LRG sample analysis further.

We now analyze the individual mocks for three cases: 1) fitting the complete range $[27.5, 127.5] h^{-1}\text{Mpc}$ using monopole and quadrupole, 2) fitting the complete range $[27.5, 127.5] h^{-1}\text{Mpc}$ using monopole, quadrupole, and hexadecapole, and 3) fitting the complete range $[27.5, 127.5] h^{-1}\text{Mpc}$ for monopole and quadrupole and reducing the range to $[47.5, 127.5] h^{-1}\text{Mpc}$ for the hexadecapole. Figure 8 show the results of the individual fits in all three cases and for the four parameters of interest $[f\sigma_8, b\sigma_8, \alpha, \epsilon]$, as well as their respective best fit distributions histograms. The colored dashed lines indicate the mean of the best fits, and the dotted line represents the expected value of the parameters. Table 4 presents the results of the individual fits for the parameters of interest.

The monopole- and quadrupole-only fits show a bias in the estimation of the three parameters of $|b_{f\sigma_8}| = 0.009$, $|b_\alpha| = 0.002$, and $|b_\epsilon| = 0.001$. The standard deviation of the distributions are $S_f = 0.052$, $S_\alpha = 0.014$, and $S_\epsilon = 0.019$ respectively; the expected values are within the dispersion. Thus the significance of the biases are 1.5σ , 1.7σ and 0.5σ . These numbers are in agreement with the test performed for the BOSS sample and these numbers are comparable with the results obtained in Alam et al. (2017a)³. The full range hexadecapole fits show a lower bias in the f parameters, with a value of $|b_{f\sigma_8}| = 0.006$, and slightly larger biases on α and ϵ with values of $|b_\alpha| = 0.004$ and $|b_\epsilon| = 0.003$ respectively. The standard deviation of the distributions decreases for f , α and ϵ , with $S_f = 0.031$, $S_\alpha = 0.013$ and $S_\epsilon = 0.011$. the significance of the biases increases significantly to 1.8σ , 2.5σ , and 2.9σ respectively. Constraining the range of hexadecapole fits, produces biases of $|b_{f\sigma_8}| = 0.013$, $|b_\alpha| = 0.001$, and $|b_\epsilon| = 0.003$, while also decreasing the standard deviation of the distributions compared with the monopole and quadrupole fits, $S_{f\sigma_8} = 0.040$, $S_\alpha = 0.012$ and $S_\epsilon = 0.013$, giving a significance of the biases of 3σ , 1σ , and 2.1σ , respectively.

Figure 9 shows the summary of the analysis for our three cases in the same format as the results reported in Alam et al. (2017a): the points correspond to the mean of the results obtained from fitting our 84 SkyCut with the BOSS mask mocks, the three quantities shown are (from left to right) the mean of $\Delta f = f - f_{\text{exp}}$, $\Delta\alpha = \alpha - \alpha_{\text{exp}}$, and $\Delta\epsilon = \epsilon - \epsilon_{\text{exp}}$, and the error indicated is the standard deviation of our fits. The panels contain the results from: 1) the fits with monopole and quadrupole (left), 2) the fits also including the hexadecapole (middle), and 3) the fits using multipoles up to $\ell = 4$ and using a constraint range on the hexadecapole (right). We also include the result for the growth factor obtained by BOSS and reported in Alam et al. (2017a) (far right value of the left panel). These results suggest that the most accurate results (smaller parameter biases in all parameters normalized by the dispersion) are obtained using the multipoles up to $\ell = 2$. Using the hexadecapole in the full range reduces the standard deviation significantly but produces larger biases.

Figure 10 displays the model behavior for variations

³ The BOSS analysis only reported the result of $\Delta f\sigma_8$ for the N-Series Mocks Challenge.

Table 3. Results from fitting the mean of N-series Mocks. The expected values for the N-series mocks are $f(z = 0.5) = 0.740$, $\alpha = 1.0$ and $\epsilon = 0.0$.

$\xi_0 + \xi_2$ with cuts in all multipoles								
Model	Range	F'	F''	f	α	ϵ	σ_{FoG}	$\chi^2/\text{d.o.f}$
$\xi_0 + \xi_2$	27.5-127.5	0.992	1.157	0.726	0.999	0.001	0.302	33/36=0.92
$\xi_0 + \xi_2 + \xi_4$ with cuts in all multipoles								
$\xi_0 + \xi_2 + \xi_4$	27.5-127.5	0.994	2.732	0.740	0.997	-0.003	3.491	244/57=4.3
$\xi_0 + \xi_2 + \xi_4$	37.5-127.5	1.036	3.898	0.708	0.998	0.001	4.311	162/51=3.1
$\xi_0 + \xi_2 + \xi_4$	42.5-127.5	1.049	4.932	0.690	0.996	-0.001	2.974	128/48=2.6
$\xi_0 + \xi_2 + \xi_4$	47.5-127.5	1.034	3.287	0.688	0.998	0.001	0.050	102/45=2.1
$\xi_0 + \xi_2 + \xi_4$ with a cut in hexadecapole only								
$\xi_0 + \xi_2 + \xi_4$	37.5-127.5	0.990	2.090	0.740	0.997	-0.002	2.841	201/55=3.6
$\xi_0 + \xi_2 + \xi_4$	47.5-127.5	0.994	1.122	0.721	1.000	0.001	0.491	154/53=2.9

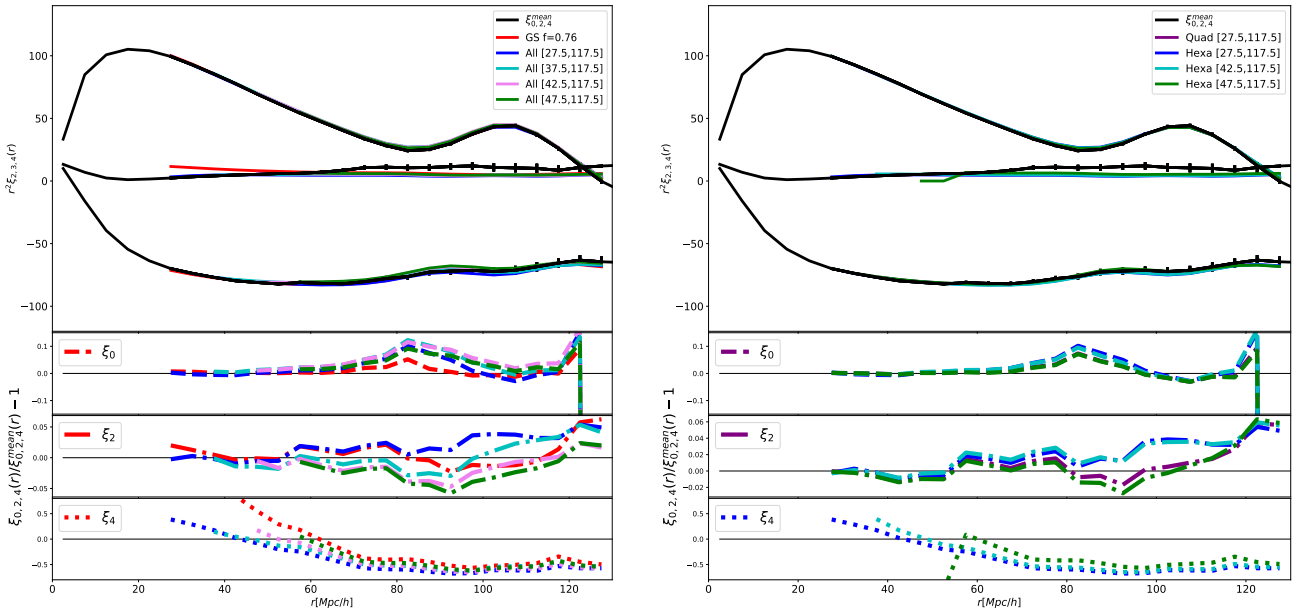


Figure 7. The mean of the mocks is shown as the black line in both plots. The error bars are computed from the re-scaled QPM mocks covariance. The left panel shows the best fit models from different lower ranges of the multipoles. In the right panel only the lower range of the hexadecapole is varied. The error plots show the quotient between the best fit model and the mean of the mocks. For all cases are residuals in the hexadecapole, the smaller residuals are obtained by the monopole + quadrupole.

of the parameters, and is included to explain the different trends observed in both sets of mocks when using multipoles up to order $\ell = 2$ compared to $\ell = 4$. We also indicate the variations in our model predicted by changes of $\sim 20\%$ in the input parameters, that correspond to deviations of $\Delta f = 0.15$, $\Delta \alpha = 0.2$, and $\Delta \epsilon = 0.2$ around the fiducial cosmology expected value. The error bars were obtained from the diagonal of the mocks covariance matrix.

The variations in ϵ have a large impact on the predicted hexadecapole at all scales (middle curve), while the variations of the hexadecapole due to variations on α and f are significantly smaller and of a comparable order of magnitude. This behavior explains why the fits are driven by ϵ when the hexadecapole is included. Considering that the error bars between 20 and 60 $h^{-1}\text{Mpc}$ are smaller, their constraining power is significantly larger. However, figure 7 shows that the model obtained using the cosmology of the

mocks does not match perfectly the mean of the hexadecapole mocks at any scale, in particular at the lower scales that, as stated, have more weight in the likelihood, this explains the poor fits we achieve when using the hexadecapole. This mismatch in the hexadecapole is pushing ϵ to higher values and as a consequence, the correlated parameters follow. Therefore, the accuracy of the model at all scales is critical for not biasing the fitted parameters.

These biases were not observed in the quasar sample. Figure 10 of Zarrouk et al. (2018) shows that 10% variations of the growth factor parameter (f) have a low impact on the CLPT-GSRSD model of the hexadecapole when compared to variations of the AP parameters. As a consequence, a small variation on the hexadecapole measurement will strongly impact the χ^2 estimator.

Zarrouk et al. (2018) analyzes the quasar clustering using a sample with a density much smaller than our LGRs

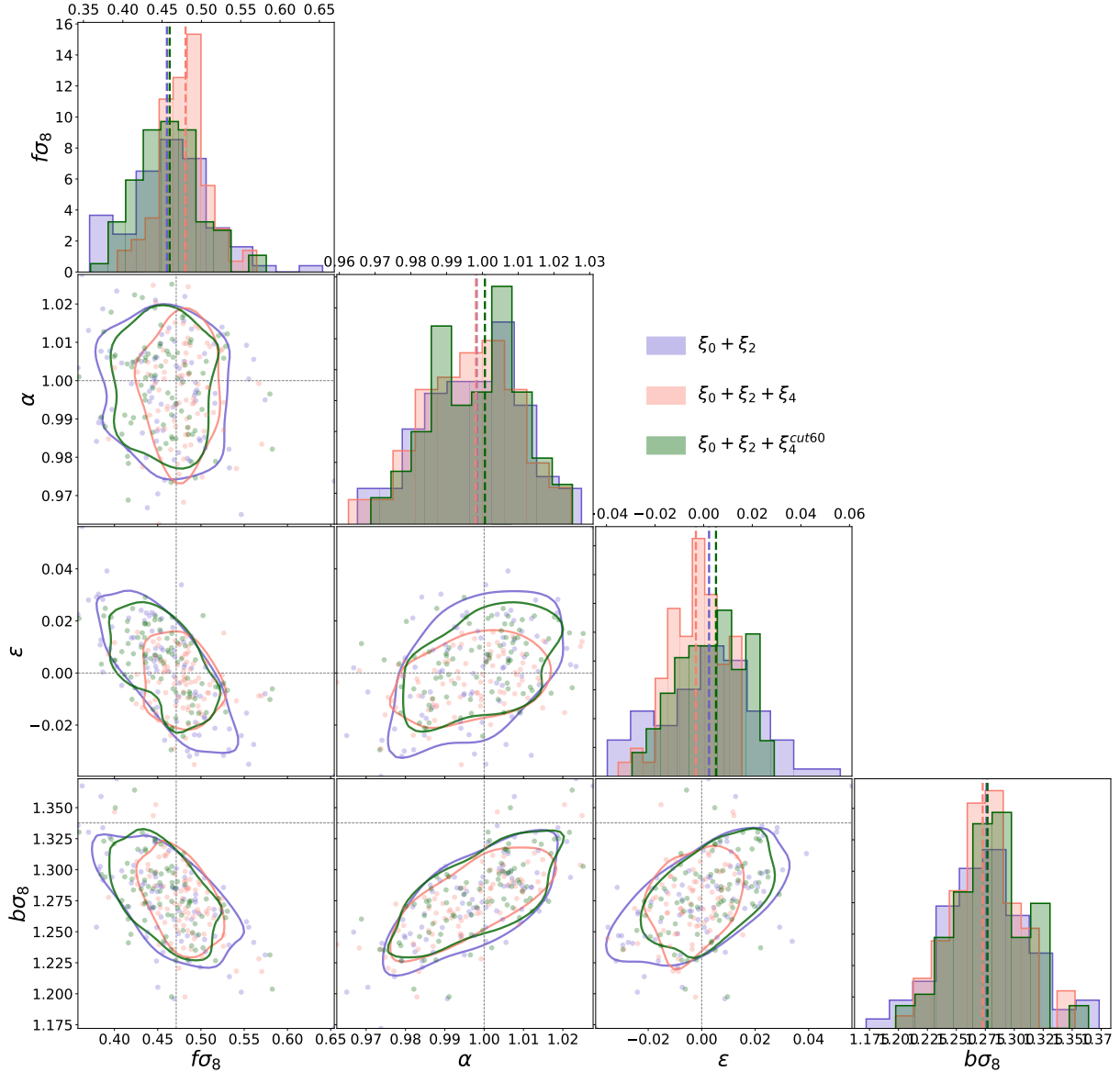


Figure 8. Results from the best fits of all of the individual mocks for the four parameters of interest $[f, b, \alpha, \epsilon]$. Also shown are their respective best fits distributions histograms and the 1σ confidence region. The dotted black lines represent the expected value of each parameter. The colored lines in each histogram indicate the mean value of that parameter found by our fits. We present three cases: 1) fitting the complete range $[27.5, 127.5] \ h^{-1}\text{Mpc}$ using monopole and quadrupole, 2) fitting the complete range $[27.5, 127.5] \ h^{-1}\text{Mpc}$ using monopole, quadrupole, and hexadecapole, and 3) fitting the complete range $[27.5, 127.5] \ h^{-1}\text{Mpc}$ for monopole and quadrupole and reducing the range to $[47.5, 127.5] \ h^{-1}\text{Mpc}$ for the hexadecapole.

sample. Their statistical error bars are larger than ours at small scales. Figure 10 shows an equivalent figure for the LRG sample but varying the value of the parameters by 20% (instead of the 10% of the Zarrouk et al. 2018 figure). We include error bars derived from our covariance matrices. This makes us more susceptible to inaccuracies in the model and to errors in our data or mocks.

6.2 Testing Systematics with eBOSS-Mocks

We will dedicate this section to test the variance of the methodology developed in Section 4. This analysis will be done using two sets of mocks, the QPM and EZ described in Section 3, both built with the same properties of our eBOSS sample. We will focus our analysis on the determination of the best fits variance, while not considering the biases due to the lack of accuracy of these mocks. The N-Series Cut-sky mocks provided an estimate of the biases on a sample that

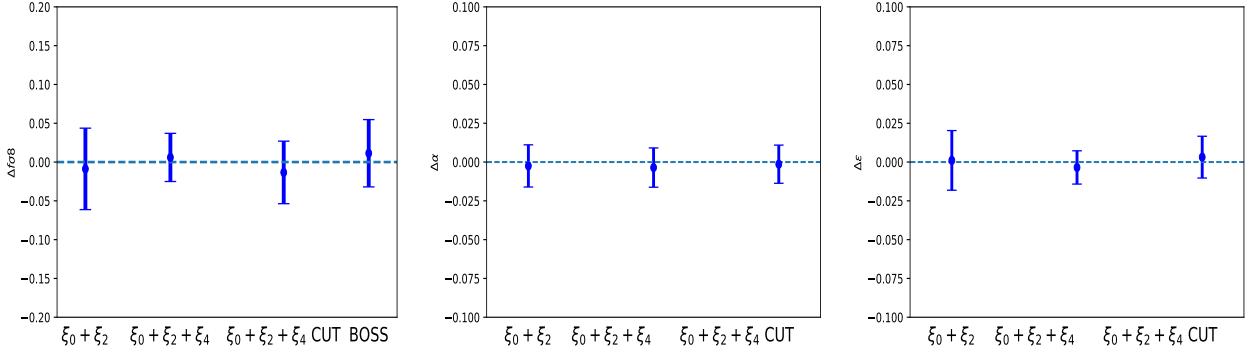


Figure 9. Systematic errors in RSD and AP parameters from using different multipole combinations in the fit. From left to right: mean of $\Delta f = f - f_{\text{exp}}$, $\Delta\alpha = \alpha - \alpha_{\text{exp}}$, and $\Delta\epsilon = \epsilon - \epsilon_{\text{exp}}$. These measurements were obtained from fitting N-Series sky mocks using two configurations: 1) multipoles up to order $\ell = 2$ and 2) multipoles up to order $\ell = 4$. The left panel includes the result from the previous work (Alam et al. 2017a). The less significant biases are obtained by the monopole + quadrupole fits. Including the hexadecapole reduces the bias and variance producing more significant bias in f and larger biases in α and ϵ .

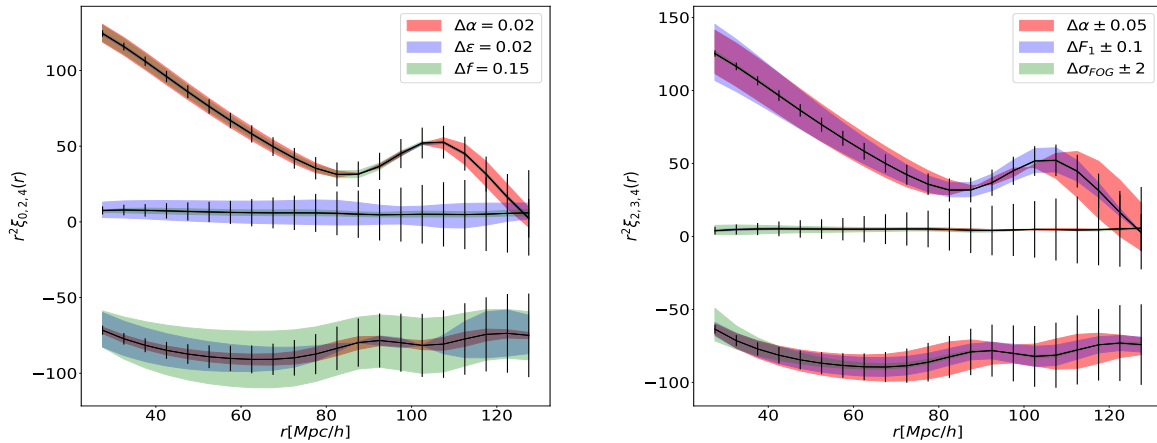


Figure 10. Left panel: Model variations for Δf , $\Delta\alpha$, and $\Delta\epsilon$ compared to the error bars coming from covariance: the behavior for the monopole (top), the hexadecapole (middle) and the quadrupole (bottom). The variations in ϵ have a large impact on the hexadecapole, while the variations in α and growth factor are of the same order of magnitude for the hexadecapole. This behavior explains why fits are driven by ϵ when the hexadecapole is taken into account. Right panel: Model variations for $\Delta F'$, $\Delta\alpha$, and $\Delta\sigma_{\text{FOG}}$ compared to the errors produced by covariance: the behavior for the monopole (top), the hexadecapole (middle) and the quadrupole (bottom).

is similar to the BOSS-LRG sample; the mean redshift was slightly lower than the one from the eBOSS LRG sample considered in this work but with similar clustering properties, i.e. the galaxy bias.

We test the CLPT-GRSD model considering six free parameters: four RSD-parameters [$f, F', F'', \sigma_{\text{FOG}}$], and two AP parameters [α, ϵ]. Our analysis was performed considering two cases: 1) Considering only the multipoles up to $\ell = 2$ (skipping the hexadecapole), and therefore following the methodology used in previous analysis performed with the LRG sample, which we will refer to as “ $\xi_0 + \xi_2$ ”. We also consider the effect of extending the multipoles up to $\ell = 4$ and ussing the full range for all multipoles, which we will refer to as “ $\xi_0 + \xi_2 + \xi_4$ ” Section 6.3 compares our results to those obtained in Bautista et al. (2018), which is a previous

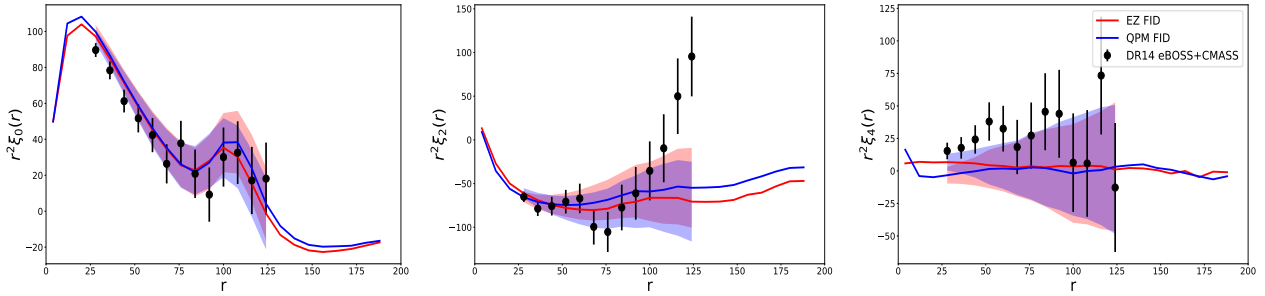
analysis using this same sample. In Section 6.4 we describe our tests of the effect of spectroscopic incompleteness and the effects of different mitigation techniques for dealing with redshift failures systematics.

The mocks were calibrated to match the data. However, as shown in Figure 11, the QPM and EZ mock have a small mismatch in the monopole at small scales. Also, both seem to systematically underestimate the hexadecapole. Keeping in mind the differences in the data with respect to the covariance mocks, we proceed to test the capacity of the model to reproduce the mocks multipoles.

We used the natural cosmology of the QPM mocks to compute their comoving coordinates, and the fiducial cosmology for computing those of the EZ mocks. Table 5 summarizes the results from our fits. The first block corresponds

Table 4. Results from fitting the 84 N-Series sky mocks with our fiducial methodology. The columns denoted by \tilde{x} are the mean, S_x denotes the standard deviation, and the bias (defined by equation 25) is denoted by b_x , with $x = f, \alpha, \epsilon$.

Results for Fiducial Methodology with N-series Sky mocks										
Model	$f\sigma_8$	S_f	b_f	$\tilde{\alpha}$	S_α	b_α	$\tilde{\epsilon}$	S_ϵ	b_ϵ	N_{mocks}
$\ell_{\max} = 2$ [27.5,117.5]	0.463	0.052	-0.009	0.998	0.014	-0.002	0.001	0.019	0.001	83
$\ell_{\max} = 4$ [27.5,117.5]	0.477	0.031	0.006	0.996	0.013	-0.004	-0.003	0.011	-0.003	81
$\ell_{\max} = 4$ [47.5,117.5]	0.458	0.040	-0.013	0.999	0.012	-0.001	0.003	0.013	0.003	83

**Figure 11.** Mean QPM/EZ mocks and DR14 correlation function, all computed in the fiducial cosmology. QPM and EZ mock underestimate the hexadecapole. The monopole (left) shows small mismatches between the mocks and the data at small scales, the quadrupole data (center) presents a large correlation in the large scale quadrupole that lies outside the 1σ variation observed in the mocks, the hexadecapole data (center) has a larger amplitude than the one predicted by the mocks.

to the monopole + quadrupole fits using the QPM/EZ mocks; the second block describes the analysis adding the hexadecapole to our fits.

The dispersions obtained from our two sets of mocks when only using the monopole and the quadrupole in the fits (first block of Table 5) are fairly consistent for all of the parameters of interest: $S_{f\sigma_8}^{\text{QPM}} = 0.113$ and $S_{f\sigma_8}^{\text{EZ}} = 0.122$, $S_\alpha^{\text{QPM}} = 0.039$ and $S_\alpha^{\text{EZ}} = 0.043$, and $S_\epsilon^{\text{QPM}} = 0.053$ and $S_\epsilon^{\text{EZ}} = 0.044$. The dispersion is also consistent with previous results found during the anisotropic LRG DR14 BAO analysis from Bautista et al. (2017) where: $S_\alpha^{\text{BAO}} = 0.048$ and $S_\epsilon^{\text{BAO}} = 0.055$.

In order to compare with the previous results from BOSS reported in Alam et al. (2017b), we need to rescale the variance using the differences in volume between the two samples; the effective volume of our sample is 0.9 Gpc^3 while BOSS-CMASS accounts for 4.1 Gpc^3 in the $[0.5, 0.75]$ redshift slice. The CMASS sample reported the following standard deviations for the $[0.5, 0.75]$ redshift slice: $S_{f\sigma_8}^{\text{BOSS}} = 0.058$, $S_\alpha^{\text{BOSS}} = 0.016$, and $S_\epsilon^{\text{BOSS}} = 0.022$ (Table 6 of Alam et al. 2017b), we can scale them roughly to the eBOSS volume using $S_X^{\text{eBOSS}} = (S_X^{\text{BOSS}} \times 4.1 \text{ Gpc}^3) / 0.9 \text{ Gpc}^3$, yielding the following scaled dispersions: $S_{f\sigma_8}^{\text{BOSS}} = 0.124$, $S_\alpha^{\text{BOSS}} = 0.034$, and $S_\epsilon^{\text{BOSS}} = 0.047$. These values are in agreement with the dispersion obtained with our QPM/EZ mocks.

Now, let us examine the fits that include the hexadecapole. The dispersion obtained from the two sets of mocks is also consistent for the parameters f and ϵ : $S_{f\sigma_8}^{\text{QPM}} = 0.090$ and $S_{f\sigma_8}^{\text{EZ}} = 0.089$, and $S_\epsilon^{\text{QPM}} = S_\epsilon^{\text{EZ}} = 0.050$ and $S_\alpha^{\text{QPM}} = S_\alpha^{\text{EZ}} = 0.028$.

Table 5 lists the mean of the differences for completeness. However, as stated before, we will not quantify biases with the approximative mocks because they do not have

the precision required to test the model; nevertheless, we report the results of the individual fits in order to demonstrate that the results are still reasonable regardless of the inaccuracies of the mocks. Figure 13 shows the distribution of the differences between the parameters of interest and their expected values on a mock-by-mock basis, i.e. $\Delta f\sigma_8 = \langle f\sigma_8 - f\sigma_{8\text{exp}} \rangle$, $\Delta\alpha = \langle \alpha - \alpha_{\text{exp}} \rangle$, $\Delta\epsilon = \langle \epsilon - \epsilon_{\text{exp}} \rangle$, and for $b = 1 + F'$, $\Delta b = \langle b\sigma_8 - b\sigma_{8\text{exp}} \rangle$, for both the analyses using multipoles up to $\ell = 2$ and up to $\ell = 4$. Reviewing the monopole + quadrupole fits (in blue) reveals that both sets of mocks show a well-behaved distribution that is centered close to zero and is symmetric. From the hexadecapole fits, the individual points and especially the 1D distributions are slightly shifted for the $f\sigma_8$ and ϵ parameters. In general we observe symmetric distributions centered in zero, except from QPM that shows a small bias in the $f\sigma_8$ parameter for the hexadecapole fits. This behavior is related to the QPM mocks poor precision at small scales and to the fact that the model and the mean multipoles present mismatches, as discussed below. The biggest mismatch between mock and model occurs in the hexadecapole for the QPM mocks and in the quadrupole for the EZ mocks.

In order to understand the distributions of the best fits, we present in Figure 12 the model template with the natural cosmology of the mocks denoted by “Model GS $f(z = 0.72)$ ”. For the QPM mocks (left panel), the model with the natural cosmology does not match the mean of the mocks (black line), this is evident in the quadrupole residuals. However, a template using a growth factor corresponding to a lower redshift ($z = 0.56$) is a better match with the mean of the mocks; this model is denoted by “Model GS $f(z = 0.56)$ ” and is shown with red dotted lines. Given that this fits were

made with the mean of the mocks, we expect the individual fits to follow this same trend.

From this analysis we can draw the following initial conclusions. First, the GSRSD model cannot match the multipoles of the QPM mocks, as they show a mismatch in the mean of the mocks and the model quadrupole, giving rise to a higher value than the input value of the simulations. Second, the model hexadecapole is systematically larger than the mean of the mocks, and in particular any conclusion about the bias of the hexadecapole cannot be extracted from the fits of the QPM mocks. We will, however, take the variance of the mocks from these distributions as a reference.

We also include a similar figure (right panel of Figure 12) for the fits done with the EZ mocks. The mean of the mocks is computed in the fiducial cosmology and shown as a black line, the model computed using the fiducial cosmology with a growth factor at the effective redshift of the mocks is represented as a red line. We also find a mismatch this time with the small scales of the quadrupole: the template with the cosmology and redshift of the mocks (red line) does not match with the mean quadrupole of the mocks (black line). It is interesting to notice that the mean hexadecapole matches the template, thus we can expect to get better fits when using the hexadecapole information. We also notice that the mismatch in the quadrupole behaves different for different scales, the scales lower than $50 h^{-1}$ Mpc are over-estimated and the scales larger than $50 h^{-1}$ Mpc are under-estimated. Thus, the EZ mocks seem to not be reproducible by the model. Apparently, the template with the mocks cosmology fits the mean better, but the template is not capable of fitting all of the scales of the quadrupole and the hexadecapole simultaneously.

The main conclusions drawn from the tests performed with N-Series/EZ/QPM are the following: the lower bins of the hexadecapole have a large constraining power, given the smaller error bars of those points. Thus including the hexadecapole is desirable, but we need to make sure that our model can reproduce both the quadrupole and hexadecapole with high accuracy at small scales. In our case, when analyzing N-Series we found that the CLPT-GSRSD model fits the monopole and quadrupole well. When using the hexadecapole, the bias in the growth factor decreases when compared to the monopole and quadrupole case, but because using the hexadecapole reduces dispersion, it becomes more significant. Additionally, the biases of α and ϵ become larger when using the hexadecapole than when we leave it out.

Given this, we decided to use the monopole + quadrupole configuration to do our data analysis, as stated this is due to the fact that the significances of the biases found are smaller, and also because we were able to study their variance with mocks that reproduce the clustering up to $\ell = 2$. Based on the results from N-Series we adopt $\sigma_{f\sigma_8}^{sys} = 0.009$, $\sigma_{\alpha}^{sys} = 0.002$, and $\sigma_{\epsilon}^{sys} = 0.001$ as an estimate of the potential bias of f , α and ϵ . Unfortunately, we do not have mocks with *eBOSS* properties capable of testing the hexadecapole methodology, we showed that the covariance mocks are not precise enough to test the hexadecapole fits. Further analyses done by DR16 should use higher accuracy mocks with *eBOSS* properties, this will allow us to revisit including the hexadecapole in our methodology.

6.3 Comparison of AP parameters results with BAO-only fits

The left panel of Figure 14 shows the difference between our FS fits and the expected value compared to those from the anisotropic BAO parameters, the later taken from Bautista et al. (2017). The dispersion for the anisotropic warping, ϵ , from BAO fits is slightly larger compared to the FS best fits. In an RSD analysis other parameters that affect the quadrupole are included (most significantly the growth factor f), so it is not surprising that FS analysis breaks some degeneracies in ϵ and reduces its dispersion. There is also a small shift in the isotropic dilation parameter, α , when comparing the FS analysis best fits to those coming from BAO. The left panel of Figure 14 shows the scatter plot for α , with a Pearson correlation factor of $r = 0.5$. There are several differences in the fitting methodology between these two fits. Obviously the modeling of the signal is different in BAO and in our RSD+AP model, but in addition the fitting range used in BAO is wider in its r -range that is extended to $180 \text{ Mpc}/h$ while our FS analysis is constrained to r -values lower than $130 \text{ Mpc}/h$. Also, the binning used in BAO is 5 Mpc in width, while this work is using bins with a width of 8 Mpc .

6.4 Testing the Impact of Spectroscopic Incompleteness

To test the effect of redshift incompleteness in our clustering, we consider three cases: the first is our mock catalogs with no redshift failures. Then, we study the effect of the two mitigations techniques described in Section 2.3.2. The redshift failures are added to the mocks by associating a position in the plate to each galaxy, then the catalog of binned probabilities is used to mimic the effect of the redshift failures observed in our data. The second case explored is the up-weighting methodology, and finally, for the third case, the forward-modeling technique.

Figure 15 displays the impact of different mitigation methods on the average of all 1000 mock catalog correlation functions. The three lines represent the case without redshift failure corrections and the up-weighting and forward modeling corrections. While the monopole is equally well recovered in all three cases, the quadrupole shows a clear shift (i.e., bias) at all scales when using the up-weighting method. The forward-modeling corrections recover the expected values for scales smaller than $r = 140 \text{ Mpc}/h$, but show slight discrepancies at larger scales.

Table 6 lists the results of the the best-fit parameters found by fitting all 100 QPM mocks using both correction schemes. We compared the results of the mocks where redshift failures are applied and corrected by one of the two mitigation techniques with the case where no redshift failures are considered. We report the difference of the mean of the best fits as an indicator of the systematic bias related to the spectroscopic completeness denoted by Δf , $\Delta \alpha$, and $\Delta \epsilon$; we also report the the dispersion S_x , where $x = f, \alpha, \epsilon$. We observe that the up-weighting technique differs from the case without redshift failures by $|\Delta f| = 0.016$ ($\Delta f / (S_f / \sqrt{N_{sim}}) \sim 0.7\sigma$), $|\Delta \alpha| = 0.001$ (0.1σ), $|\Delta \epsilon| = 0.003$ (0.7σ). When using the forward modeling, the systematic error reduces to $|\Delta f| = 0.004$ (0.1σ), $|\Delta \alpha| = < 0.001$ ($< 0.1\sigma$)

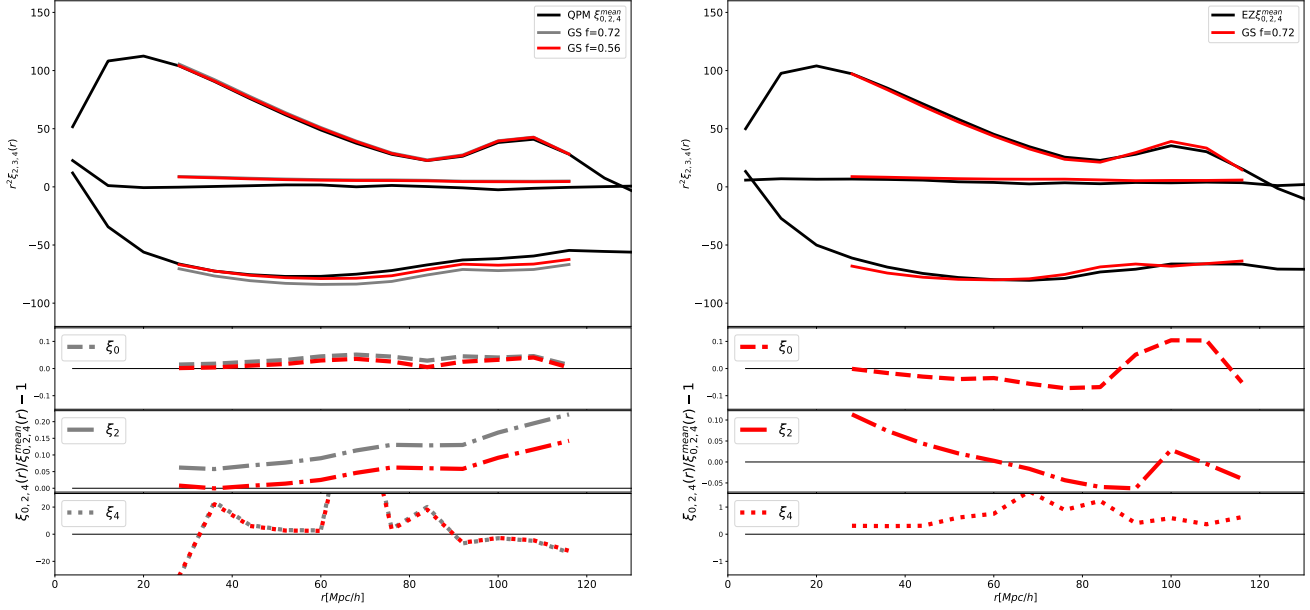


Figure 12. Mean QPM/EZ mocks vs. Template with Mock Cosmology. The error bars are smaller than the size of the points. For QPM mocks, the template with the mocks cosmology does not match the mean of the mocks (black line), this is evident in the quadrupole and hexadecapole residuals. For the EZ mocks, the template with the mocks cosmology fits the mean better, but the template does not match all of the scales of the quadrupole and the hexadecapole simultaneously.

Table 5. Results from fitting the 100 QPM/EZ mocks for FS analysis. We include the analysis for both cases using the hexadecapole in addition to the monopole and quadrupole. The columns denoted by \bar{x} are the mean, and the S_x denotes the standard deviation. The variables are the difference of the parameters of interest compared to their expected values on a mock-by-mock basis, i.e. $\Delta f\sigma_8 = \langle f\sigma_8 - f\sigma_{8\text{exp}} \rangle$, $\Delta\alpha = \langle \alpha - \alpha_{\text{exp}} \rangle$, $\Delta\epsilon = \langle \epsilon - \epsilon_{\text{exp}} \rangle$, for both the analysis using multipoles up to $\ell = 2$ and using multipoles up to $\ell = 4$.

Model	Monopole-Quadrupole fits						$\chi^2/\text{d.o.f}$	N_{mock}
	$\Delta f\sigma_8$	$S_{\Delta f\sigma_8}$	$\bar{\Delta\alpha}$	$S_{\Delta\alpha}$	$\bar{\Delta\epsilon}$	$S_{\Delta\epsilon}$		
FS-QPM MQ	-0.036	0.113	0.003	0.039	0.006	0.053	1.0	97
FZ-EZ MQ	-0.007	0.122	0.009	0.043	0.001	0.044	1.0	91
Model	Including Hexadecapole						$\chi^2/\text{d.o.f}$	N_{mock}
	$\Delta f\sigma_8$	$S_{\Delta f\sigma_8}$	$\bar{\Delta\alpha}$	$S_{\Delta\alpha}$	$\bar{\Delta\epsilon}$	$S_{\Delta\epsilon}$		
FS-QPM	-0.018	0.090	-0.011	0.050	0.009	0.028	1.1	84
FS-EZ	-0.024	0.089	0.005	0.050	0.008	0.028	1.0	97

and $|\Delta\epsilon| = 0.005$ (0.8σ). There is an increase of the dispersion for the case of the up-weighting technique in the parameters f and ϵ , which decreases for f for the forward modeling scheme but is still larger when compared to the case without redshift failures, but increases the shift by 0.002 on ϵ . In any cases the biases are less than 1σ . Given these results, we conclude that the forward modeling scheme performs slightly better than the up-weighting scheme. Therefore, in the rest of our analysis, we will adopt the forward modeling scheme for correcting the redshift failures.

7 RESULTS ON THE LRG DR14 SAMPLE

We performed the analysis on the eBOSS-CMASS sample combining the NGC and SGC (if not otherwise stated). The covariance matrices used in our fits were rescaled by a factor of 0.9753 in order to account for the slight mismatch between the footprint area of the data and of the mocks. Before running a full Monte Carlo Markov Chains (MCMC) analysis, we first tested the robustness of our measurements by using the maximum likelihood method described in the last section. While these results were not expected to provide any information on the confidence contours of our parameters (as an MCMC would), they give an idea of the maximum likelihood values. The main reason for performing these tests is that our MCMC analysis in its current implementation is

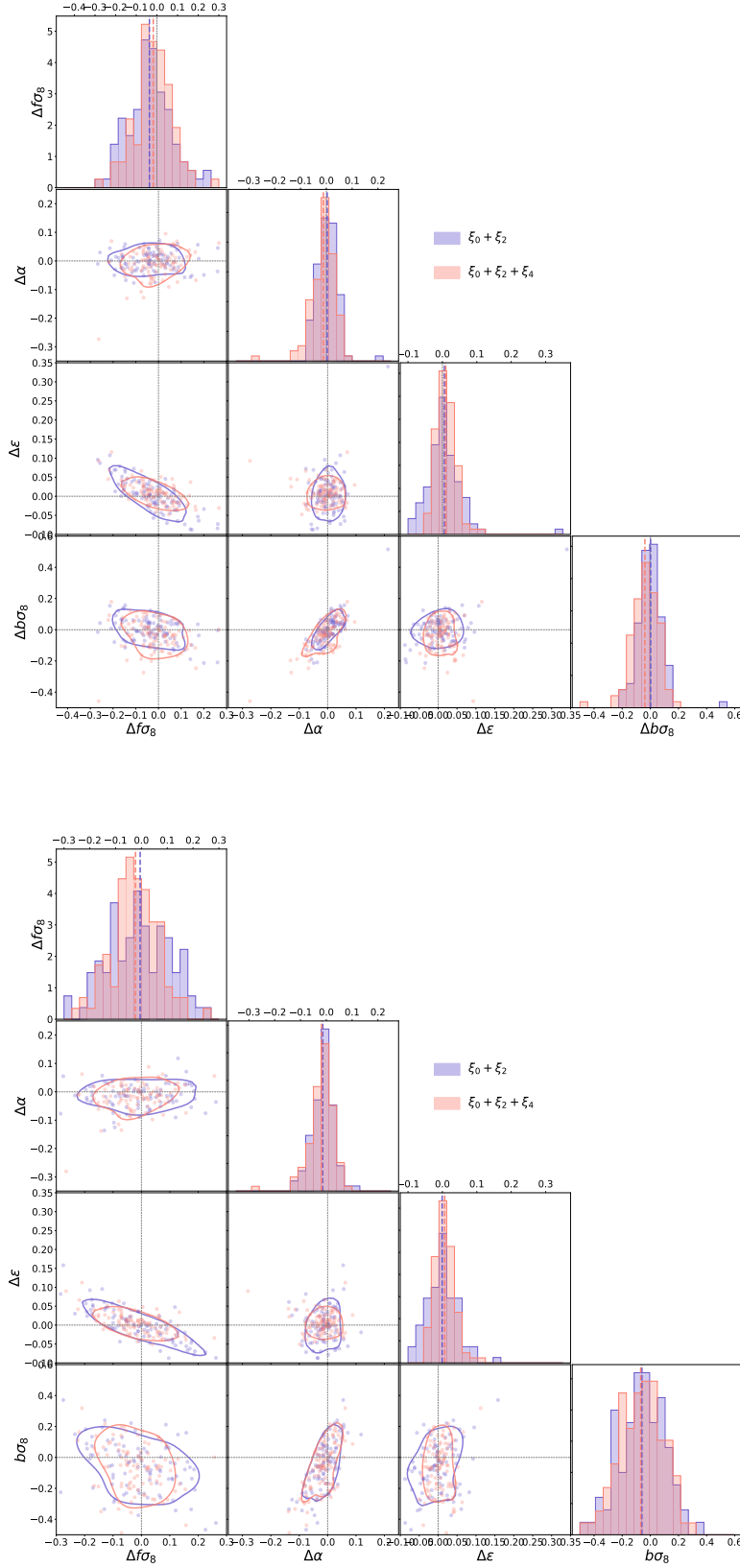


Figure 13. Scatter triangle plots comparing fits for full shape fits using $\xi_0 + \xi_2$ and $\xi_0 + \xi_2 + \xi_4$ for QPM (up) and EZ (down) mocks. We show the difference of the best fit values with respect to the expected values for each of the parameters of interest. The means are indicated as solid lines for the three cases explored. The dotted lines indicate the expected values, which are zero for all cases.

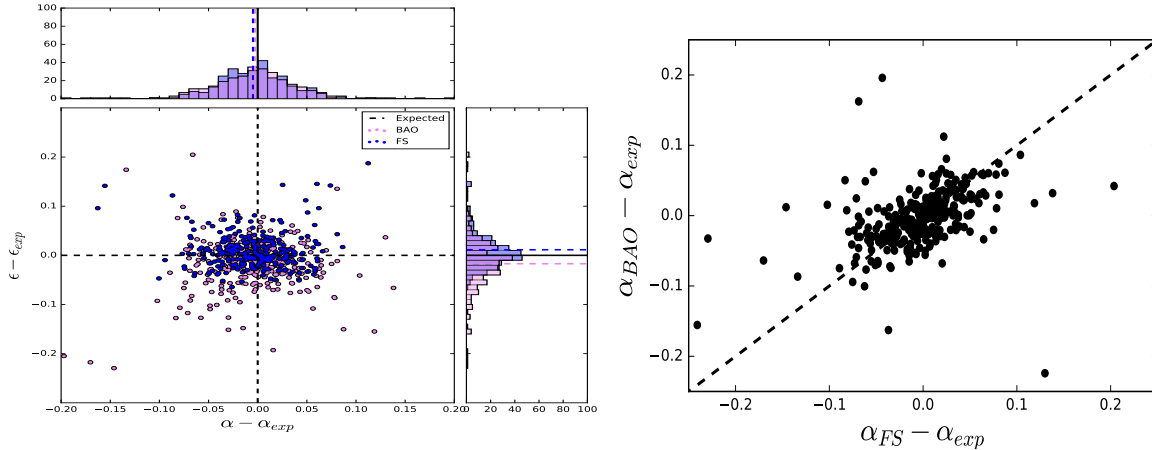


Figure 14. Left panel: A comparison of the BAO fits and full shape using $\xi_0 + \xi_2$ for the mocks. Right panel: comparison of best fits in isotropic dilation parameter for FS and BAO for the mocks. The dispersion for the anisotropic warping, ϵ , from BAO fits is slightly larger compared to the FS best fits. FS analysis breaks some degeneracies in ϵ and reduces its dispersion.

Table 6. Testing for Redshift Failures. Fitting results from 100 QPM mocks using two different techniques for mitigating the redshift failures. We compared the results of the the mocks where redshift failures are applied and corrected by one of the two mitigation techniques to the case where no redshift failures are considered. We report the difference of the mean of the best fits as an indicator of the bias related to the spectroscopic completeness denoted by Δf , $\Delta \alpha$, $\Delta \epsilon$ and we also report the dispersion by ΔS_x , where $x = f, \alpha, \epsilon$.

Testing Impact of Mitigation Techniques for Redshift Failures.									
Mitigation Methodology	Δf	S_f	$\Delta \alpha$	S_α	$\Delta \epsilon$	S_ϵ	$\Delta F'$	$\Delta F''$	$\Delta \sigma_{FOG}$
No Fiber Collisions	-	0.232	-	0.113	-	0.050	-	-	-
Forward Modeling	+0.003	0.252	<-0.001	0.116	+0.005	0.061	0.005	0.394	-0.271
Fiber Weights	-0.016	0.250	-0.001	0.112	+0.003	0.054	<0.001	-0.141	-0.234

prohibitively time-consuming; we simply can not afford to run all the tests on our data using a full MCMC approach. Further development needs to be done in order to reduce the time of convergence of our final analysis. These maximum likelihood tests can also be used as a check of the robustness of our MCMC results.

Our first test compares the robustness of the fit against variations in the maximum fitting range (the maximum distance in $h^{-1}\text{Mpc}$ where the correlation function is measured). This test is particularly important in our analysis. Figure 5 shows that the quadrupole estimates made with the data show large correlation estimates larger than 100 $h^{-1}\text{Mpc}$, which are outside the variance observed in the mocks. This anomalous correlation at large scales affects the capability of our model to fit the data multipoles. We suspect this behavior could be related to an unknown systematic or a statistical fluctuation. Given that we could not identify any systematic that affects the quadrupole, and that we can not exclude a large fluctuation, we also analyzed the behavior of the fits when those large scales are eliminated in all multipoles with $\ell \geq 2$. Our main result, however, is quoted with the complete range. If this behavior is repeated in the DR16 analysis, that will indicate a systematic error that needs to be analyzed properly to provide non-biased results. If the origin of this correlation is a statistical fluctuation, this feature will probably be diluted with an increase in volume.

Thus, before exploring the likelihood surface, we performed some maximum likelihood fits using a variety of

ranges. The fiducial case uses the complete range between $[28, 124]h^{-1}\text{Mpc}$ for the multipoles up to $\ell = 0, 2, 4$. We also tested some variants of this range to investigate the impact of cutting the large scale of each multipole on the best fits.

Table 7 lists the results of the best fits for the fiducial cases and several variants and figure 16 shows how the best fit models compare to the data. From table 7, we conclude that reducing the range of the fit from 128 to 92 $h^{-1}\text{Mpc}$ improves the goodness of the fit for both the monopole+quadrupole fit and the monopole+quadrupole+hexadecapole fit. The $\chi^2/\text{d.o.f.}$, a measurement of the goodness of a fit, reduces from 2.1 to 1.35 for the $\ell_{max} = 2$ case (However, there is no reduction when we reduce the range for both monopole and quadrupole where $\chi^2/\text{d.o.f.}$ stays at 2.09), and from 1.81 to 1.16 if we eliminate large scales for all $\ell = 0, 2, 4$ (It stays the same if we only limit hexadecapole, 1.14 if we restrict the range of the large scales for both $\ell = 2, 4$ but not for the monopole). By using the complete range we increase the discrepancy between the fits using different order multipoles (i.e. $\ell_{max} = 2$ versus $\ell_{max} = 4$). The difference in the best fit parameters for the growth factor f is 0.211 for the complete ranges (row one minus two), and it becomes 0.139 when reducing the quadrupole and hexadecapole ranges to $[28, 92]h^{-1}\text{Mpc}$ (row three minus six). Similar trends occur with ϵ , where the differences in the best fit values range from 0.064 to 0.042. These trends indicate that the large correlation observed in the quadrupole is not properly modeled by our

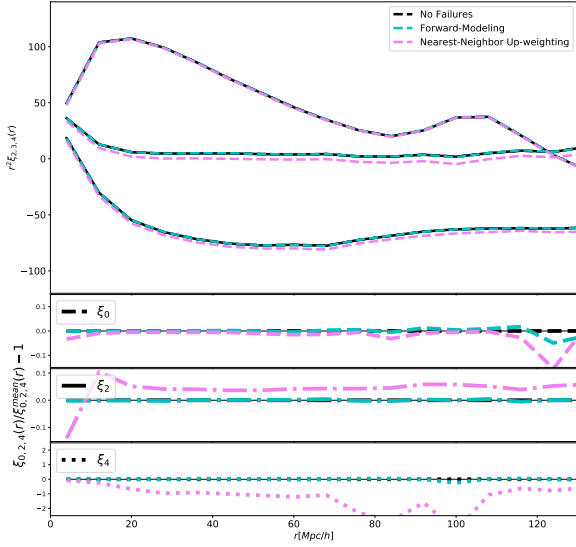


Figure 15. Impact of the redshift completeness on the multipoles and the effect of the mitigation techniques for correcting potential biases. The monopole (top), the quadrupole (bottom) and hexadecapole (middle) are presented in three cases: without redshift failures, correcting by the up-weighting technique, and correcting using the Forward modeling technique. While the monopole is well recovered by the two correction techniques, the quadrupole/hexadecapole shows a clear shift (i.e., bias) at all scales when corrected with the up-weighting method. The forward-modeling recovers the expected values for scales smaller than $r = 140$ Mpc/h.

CLPT-GSRSD template. When we exclude the large scales of the monopole, there is a significant shift in both f and ϵ , with f shifting from 0.905 to 0.589 and ϵ from -0.026 to 0.088 . These shifts are expected when eliminating the large scales on the monopole. Finally, excluding the large scales on the hexadecapole affects the f fits, and mildly affects the ϵ fits, as the quadrupole and hexadecapole capacity to break the degeneracy between f and ϵ is derived from the BAO scales. The goodness of the fit, $\chi^2/\text{d.o.f.}$, improves when removing the large scales, due to the incapability of modeling the anomalous correlation; this approach loses all the information encoded in the BAO in the quadrupole and hexadecapole. Consequentially, the results for the AP parameters are degraded and potentially biased. We will perform the MCMC exploration for the same four cases for completeness, but we will quote the full range as our final result.

As stated, we used an MCMC methodology for exploring the likelihood surface, which was done using the Monte Python public code (Audren et al. 2013). We use flat priors for our parameters; the range of these priors is presented in Table 8. We run two different chains in the combined data set (NGC+SGC). The first is with the monopole and quadrupole only ($\xi_0 + \xi_2$) and using the fiducial distance range. The second chain also runs with the monopole and quadrupole ($\xi_0 + \xi_2$), but restricting the range in the

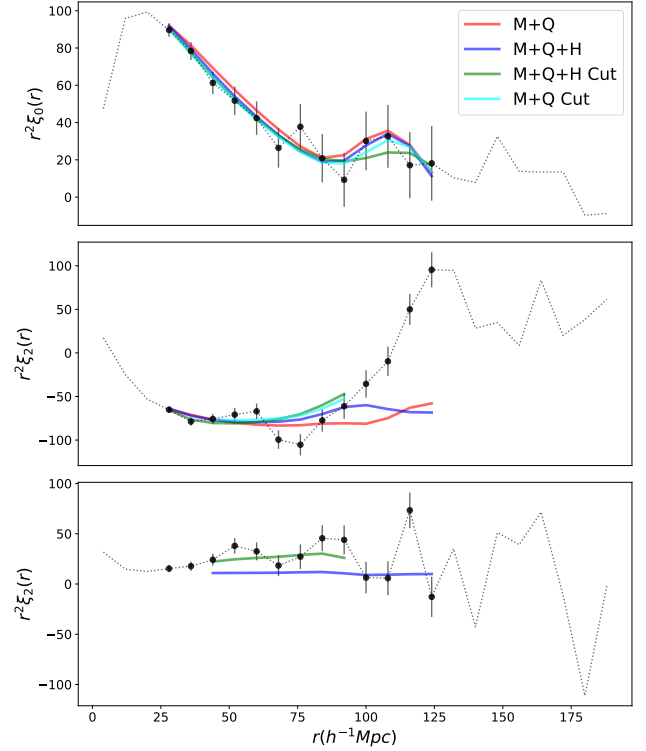


Figure 16. The maximum likelihood model for four cases: 1) using multipoles up to $\ell = 2$ in the fiducial range, 2) using multipoles up to $\ell = 4$ for the fiducial range, 3) using multipoles up to $\ell = 2$ but restricting the quadrupole range to $[28, 92] h^{-1}\text{Mpc}$, and 4) using multipoles up to $\ell = 4$ but restricting the range of the quadrupole and hexadecapole to $[28, 92] h^{-1}\text{Mpc}$.

quadrupole to $[28, 92] h^{-1}\text{Mpc}$ (the monopole stays in the same range of $[28, 124] h^{-1}\text{Mpc}$). Table 9 displays the results from the MCMC analysis. Our final measurement was performed on the *combined* sample, which includes the NGC and the SGC, and was done using the fiducial methodology (i.e., $8 h^{-1}\text{Mpc}$ bins on the fiducial range). The first block reports the final result of this work, the monopole and quadrupole-only fits. The second block is for the $\xi_0 + \xi_2$ fits when excluding the large scales of the quadrupole. The third block lists the results for the Galactic hemispheres separately, this is shown for identification of any residual systematics in the data; we will discuss these results at the end of this subsection. The final block is quoted as a reference and it shows the fits of the BAO-only analysis done with this same sample in Bautista et al. (2018). MCMC chains using the hexadecapole are included for completeness in Appendix B as a robustness test, but it is not part of our main results.

Figure 17 shows the likelihood surfaces for the two runs over the $\xi_0 + \xi_2$, one chain is in the fiducial range and the other is eliminating the large scales for the quadrupole, i.e. $[28, 92] h^{-1}\text{Mpc}$. The latter is added for completeness, but as stated before, our final result will be quoted using the full range. The figure contains the $1 - 2\sigma$ confidence contours for the growth factor $f\sigma_8$, the linear bias $b\sigma_8$, the dilation parameter α , and the warping parameter ϵ , together with their marginalized 1D distributions. The $1-\sigma$ regions are fully contained inside our priors for both cases. How-

Table 7. Best Fits from Maximum Likelihood Fits for different scenarios: using the fiducial ranges for the multipoles up to $\ell = 2$ (first line), using multipoles up to $\ell = 4$ (second line), and systematically excluding the large scales for the different multipoles considered in the fits (lines three to seven).

Best Fits from Maximum Likelihood for LRG sample DR14								
Varying maximum range and ℓ								
model	range ($h^{-1}\text{Mpc}$)	F'	F''	f	α	ϵ	σ_{FOG}	χ^2
$\xi_0 + \xi_2$	[28,124][28,124]	1.005	0.74	0.905	0.947	-0.026	0.009	42.4/20=2.1
$\xi_0 + \xi_2 + \xi_4$	[28,124][28,124][28,124]	1.05	-2.7	0.694	0.965	0.038	-1.51	59.81/33=1.81
$\xi_0 + \xi_2$	[28,124][28, 92]	0.91	-3.28	0.710	0.935	0.050	2.48	24.3/18=1.35
$\xi_0 + \xi_2$	[28,92][28, 92]	0.753	-3.73	0.589	0.874	0.088	4.21	25.13/12=2.09
$\xi_0 + \xi_2 + \xi_4$	[28,124][28,124][28,92]	1.07	-2.58	0.690	0.969	0.038	0.96	52.0/29=1.79
$\xi_0 + \xi_2 + \xi_4$	[28,124][28, 92][28,92]	0.937	-2.96	0.571	0.92	0.092	5.07	28.6/23=1.14
$\xi_0 + \xi_2 + \xi_4$	[28,92][28, 92][28,92]	0.73	-3.79	0.508	0.858	0.120	6.49	24.34/21=1.16

Table 8. Flat priors ranges on the parameters of the model.

Measurements with LRG sample DR14.	
f	[0.0,2.0]
F'	[0.0,3.0]
F''	[-15,15]
σ_{FOG}	[0,40]
α	[0.8,1.2]
ϵ	[-0.2,0.2]

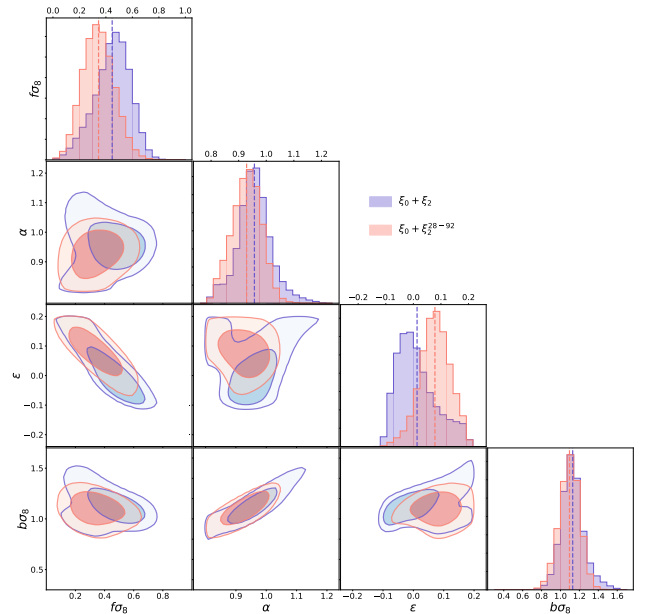
ever, the $2\text{-}\sigma$ regions are cut by our prior to large values of ϵ and small values of α , our reasons for not using larger priors on the Alcock-Paczynski parameters will be discussed in the Appendix A.

The results of $f\sigma_8$ and α are consistent within 1σ , for both ranges. However, given the anti-correlation between the ϵ and f parameters and the fact that the quadrupole is dominated by ϵ at the larger scales, when including the larger bins of the quadrupole the ϵ is driven from its expected value and as a consequence f shifts as well. When the last three bins of the quadrupole are avoided we achieve a significant improvement in the goodness of the fit towards ~ 1 ; the price paid for this approach is to eliminate the BAO information. This increases the degeneration of the parameters and biases the results, thus we lose information that constrains ϵ , which in turn causes the contour areas to become larger, providing more freedom to the fitter to move f to lower values (Figures 17).

Figure 18 displays the best-fit anisotropic models compared to the data for our fiducial choice of analysis. As expected, the monopole and quadrupole are visually good fits for the data, except for the large scales of the quadrupole where the correlation becomes strongly positive (scales larger than $90 h^{-1}\text{Mpc}$).

To finalize this section, we analyze separately the North Galactic Cap (NGC) and the South Galactic Cap (SGC). Figure 20 displays the 1σ and 2σ confidence contours obtained from running an MCMC analysis separately on both hemispheres. They are computed using our standard priors quoted in Table 8. The contours in both galactic caps are poorly defined and the 1σ interval in ϵ and α are sharply cut by our imposed priors.

As discussed in appendix A our methodology has difficulty on fixing the Alcock-Paczynski parameters to a unique value given the size of our errors compared to the strength of the BAO signal, this leads to unphysical values of ϵ and α (and therefore f due to their correlation with

**Figure 17.** The shaded regions show the $1 - 2\sigma$ confidence surfaces found by our MCMC chains for the RSD-AP parameters for the $\xi_0 + \xi_2$ space in the fiducial range (blue) and when excluding the large scales in quadrupole (red). The confidence contours for the growth factor $f\sigma_8$, the linear bias $b\sigma_8$, the dilatation parameter α , and the warping parameter ϵ are indicated, along with their 1D distributions. The dashed lines of each histogram are the mean values found by the MCMC chain.

ϵ) being accepted by the MCMC chain and affects all of the constraints of our parameters.

Given that the errors are larger for the North and the South separately than in the combined sample, the degeneration is stronger. This leads to several regions being accepted to within $1\text{-}\sigma$ that would otherwise be rejected due to their inability to reproduce the BAO peak. More data will tend to reduce this behavior and that is in fact what we see in the combined sample, where the errors are smaller.

Figure 19 presents the data multipoles for the NGC (blue points) and SGC (red points); the error bars correspond to their $1\text{-}\sigma$ variance from the sample covariance matrix computed using the QPM mocks. The blue solid line

Table 9. Results for the DR14 LRG sample. The first block is for our fiducial methodology, using the fiducial range for the $\xi_0 + \xi_2$ fit. The second block is for the $\xi_0 + \xi_2$ fits when excluding the large scales of the quadrupole. The third block shows the fits separating the hemispheres NGC and SGC and using $\xi_0 + \xi_2$ in the fiducial range. The fiducial value for the $\sigma_8(z_{eff}=0.72) = 0.55$. The eulerian bias is defined as $b = 1 + F'$.

Measurements with LRG sample DR14 Oficial Version.						
Case	$f\sigma_8$	$b\sigma_8$	$\langle F' \rangle$	σ_{FOG}	α	ϵ
$\xi_0 + \xi_2$ [28,124][28,124]	$0.454^{+0.119}_{-0.140}$	$1.110^{+0.116}_{-0.100}$	$2.245^{+3.849}_{-4.35}$	$3.713^{+2.987}_{-2.31}$	$0.955^{+0.055}_{-0.05}$	$-4e-04^{+0.090}_{-0.050}$
$\xi_0 + \xi_2$ [28, 124][28, 92]	$0.337^{+0.121}_{-0.110}$	$1.088^{+0.101}_{-0.100}$	$-1.19^{+4.002}_{-2.900}$	$5.027^{+2.721}_{-2.870}$	$0.930^{+0.050}_{-0.050}$	$0.083^{+0.059}_{-0.06}$
$\xi_0 + \xi_2$ NGC	$0.598^{+0.150}_{-0.190}$	$1.262^{+0.121}_{-0.150}$	$4.372^{+3.657}_{-5.810}$	$3.008^{+2.740}_{-1.940}$	$1.103^{+0.066}_{-0.100}$	$-0.05^{+0.085}_{-0.040}$
$\xi_0 + \xi_2$ SGC	$0.359^{+0.168}_{-0.16}$	$1.119^{+0.169}_{-0.12}$	$0.328^{+1.725}_{-1.96}$	$4.783^{+3.732}_{-3.00}$	$0.929^{+0.087}_{-0.07}$	$0.077^{+0.081}_{-0.07}$
Measurements BAO-only with LRG sample DR14 from Bautista et al 2018. Range of fits [32,182] and 8 Mpc/h bin size.						
Case	range	α_{\perp}	α_{\parallel}	corr	α	ϵ
Anisotropic	26-178	$1.01^{+0.08}_{-0.05}$	$0.82^{+0.09}_{-0.08}$	-0.39	$0.942^{+0.048}_{-0.024}$	$-0.067^{+0.033}_{-0.022}$

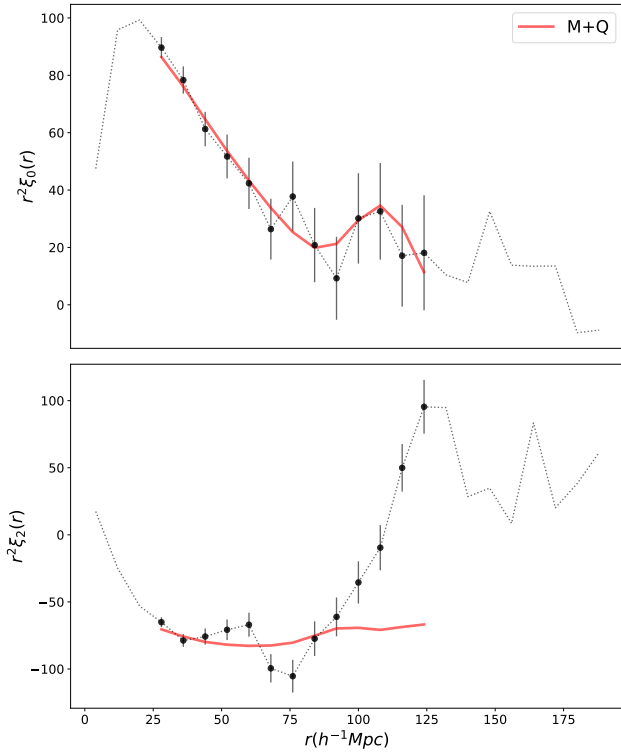


Figure 18. This plot shows how our data (black dots) compares to our model (red line). The model is built using the values from the first line of table 9, that were computed using multipoles up to $\ell = 2$ and our combined sample (NGC+SGC) in the fiducial range. The model is visually a good fit for the data, except for the large scales of the hexadecapole.

represents the fits made by our MCMC analysis in the NGC, the red solid line is the analog for the South Galactic Cap. These fits are done using the mean values obtained by our MCMC chains, which we use as our estimates of the best fits. The NGC and SGC have a significant difference in the clustering amplitude at small scales, and the peak is shifted in one hemisphere compared with the other (it is not well defined in either of the hemispheres). Both models reasonably reproduce the multipoles; this is especially true in the

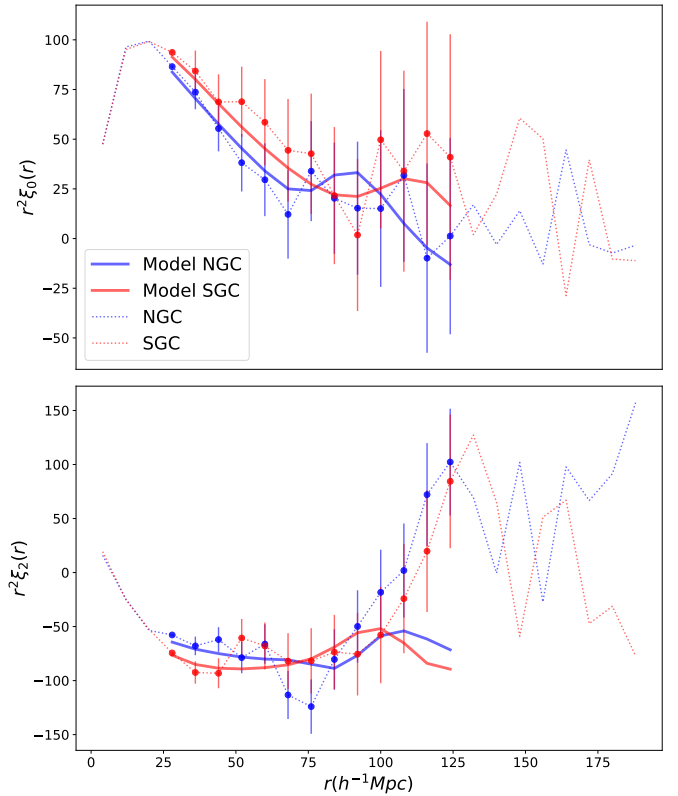


Figure 19. The blue and red dots represent the NGC and the SGC measured data points for the Monopole (top) and the Quadrupole (bottom). The errors bars are the standard deviation computed using the QPM mocks. The solid lines indicates the best model found by the MCMC for the NGC/SGC.

smaller scales which are the ones with more weight in the fit (due to their smaller variance). There is a difference in the multipole amplitude between both galactic caps, as a consequence the contours in figure 20 are displaced among each other, the results for the combined sample surrounds the regions where both contours intercept (see table 9).

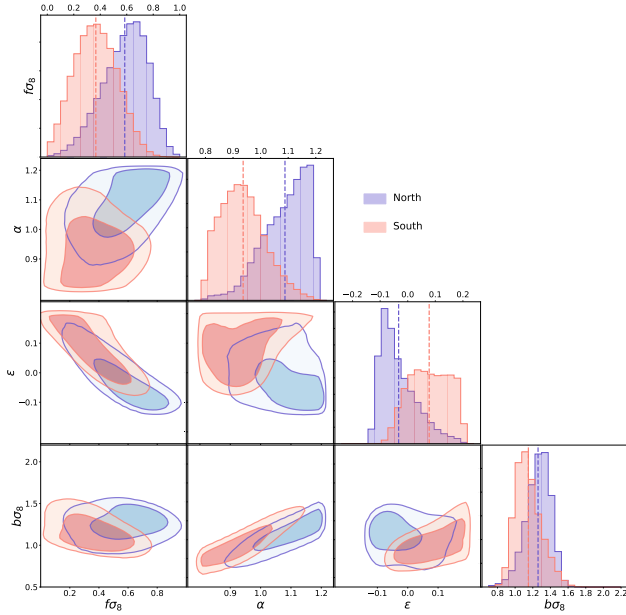


Figure 20. Equivalent to Figure 17 but presenting the MCMC chains for the RSD-AP parameters in the NGC (blue) and in the SGC (red); both of them are in the fiducial range.

8 COSMOLOGICAL IMPLICATIONS

Table 10 presents our final constraints on the growth factor $f\sigma_8$, the angular diameter distance $D_A(z)$, and the Hubble parameter $H(z)$ including the statistical and the systematic error⁴. Our fiducial cosmology was used to convert the best-fit dilation parameters $\alpha_{||}$ and α_{\perp} , into distance measurements. The table includes the same variants of the methodology quoted in table 9 for the combined sample, and the values are in agreement with each other within 1σ .

Our final constraint, the logarithmic growth of structure multiplied by the amplitude of dark matter density fluctuations, is $f(z_{eff})\sigma_8(z_{eff}) = 0.454 \pm 0.139$. Using the the Alcock-Paczynski dilation scales allowing us to constrain the angular diameter distance and the Hubble distance we arrive to: $D_A(z_{eff}) = 1466.5 \pm 136.6(r_s/r_s^{fid})$ and $H(z_{eff}) = 105.8 \pm 16(r_s^{fid}/r_s)\text{km.s}^{-1}.\text{Mpc}^{-1}$ where r_s is the sound horizon at the end of the baryon drag epoch and r_s^{fid} is its value in the fiducial cosmology at an effective redshift $z_{eff} = 0.72$. These measurements correspond to relative errors of 30.5%, 9.3%, and 15.1%, respectively considering the systematic error.

Bautista et al. (2018)’s analysis with the DR14 LRG sample reported a low statistical power of the current sample, and generated anisotropic BAO results yielded slightly worse results than isotropic fits. Further data releases from eBOSS should increase the statistical significance of our measurements.

Figure 21 presents our measurements compared with previous results from SDSS-III-BOSS DR12 from both

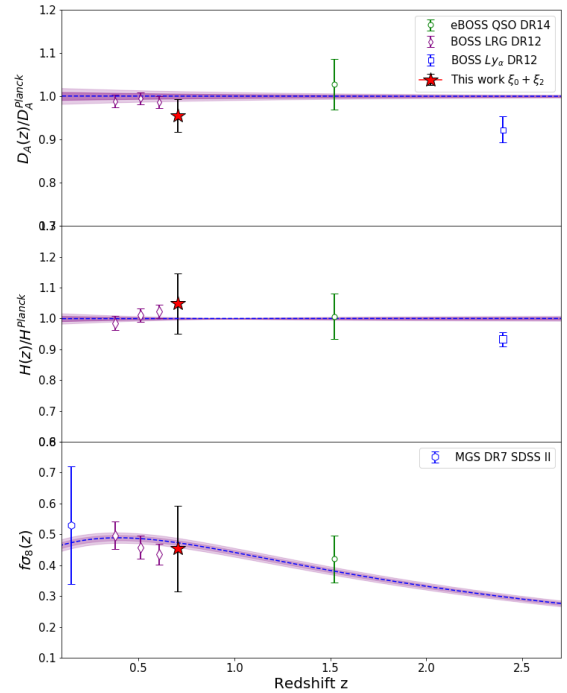


Figure 21. Measurements from DR14 eBOSS-CMASS sample using multipoles up to $\ell = 2$ (red star) fitting in the range $[24, 128] h^{-1}\text{Mpc}$.

galaxies (Alam et al. 2017a) and Lyman-alpha quasars (Bautista et al. 2017; du Mas des Bourboux et al. 2017), the eBOSS quasar measurements from Gil-Marín et al. (2018); Zarrouk et al. (2018); Hou et al. (2018)⁵, and the Main Galaxy Sample (MGS) from SDSS-II-DR7 (Ross et al. 2015). Our measurements are consistent with previous analyses and the ΛCDM model.

Our measurements with the CMASS-eBOSS sample are correlated with the CMASS measurements. The correlation coefficient between the two measurements was roughly estimated to be 0.16 (Bautista et al. 2018); a proper measurement of this correlation will be achieved for the DR16 analysis.

Finally, in order to validate our results, we compute a forecast for the joint BAO and RSD parameters using LRG DR14 samples. The observed galaxy power spectrum is modeled as in Ballinger et al. (1996); Simpson & Peacock (2010)

⁵ Figure 21 quotes the (Gil-Marín et al. 2018) result; however, the three measurements from the different analyses were shown to be fully consistent.

⁴ The systematic error is based on the results from N-Series.

Table 10. Cosmological constraints on DR14 LRG sample, using $D_A(z = 0.72)^{fid} = 1535$, $H(z = 0.72)^{fid} = 101$.

Measurements with LRG sample DR14.						
Model	range ($h^{-1}\text{Mpc}$)	α_{\parallel}	α_{\perp}	$f\sigma_8$	$D_A(z)(r_s^{fid}/r_s)$	$H(z)(r_s/r_s^{fid})$
$\xi_0 + \xi_2$	[28,124][28,124]	0.954 ± 0.151	0.955 ± 0.085	0.454 ± 0.139	1466.5 ± 136.6	105.8 ± 16
Forecast.						
-	-	0.707	0.0382	0.0271	0.0538	
BAO-only						
$\xi_0 + \xi_2$	[32,182]	0.72	0.82 ± 0.085	1.1 ± 0.065	-	

using the following equation:

$$P_{gg}^{\text{obs}}(k, \mu) = \frac{1}{\alpha_{\parallel}\alpha_{\perp}^2} \left[b\sigma_8(z) + \frac{f\sigma_8(z)\mu^2}{A^2 + (1 - A^2)\mu^2} \right]^2 \times \frac{P_{mm,z=0} \left[\frac{k}{\alpha_{\perp}} \sqrt{1 + \left(\frac{1}{A^2} - 1\right)\mu^2} \right]}{\sigma_{8,z=0}^2} + \frac{1}{n}, \quad (26)$$

where $A = \alpha_{\parallel}/\alpha_{\perp}$ denotes the relative distortion in the radial and transverse directions due to the AP effect. P_{mm} and P_{gg} are, respectively, the matter and galaxy power spectrum; n is the number density of the galaxies. The uncertainties on the BAO and RSD parameters are estimated by computing the Fisher matrix from the observed galaxy power spectrum, F_{ij} , following Tegmark (1997) with the parameter set $\mathbf{p} \equiv \{\ln(\alpha_{\parallel}), \ln(\alpha_{\perp}), \ln(b\sigma_8), \ln(f\sigma_8)\}$. In order to account for the error induced by redshift uncertainties, we multiply the integrand of F_{ij} by a damping factor of $\exp[-(k\mu\sigma_r)^2]$, where $\sigma_r = \partial r / \partial z \sigma_z$ and r is the comoving distance.

The second block of Table 10 lists the forecast when including the AP test. The measurements of $H(z)$, D_A , and $f\sigma_8$ are respectively 3.9, 3.1, and 2.6 times larger than the predictions. While this result might be caused by the non-uniform footprint of the sample at its current state, the BAO measurements also reported errors larger than the predictions.

9 CONCLUSIONS

The RSD effect generates an artificial anisotropy on the clustering of galaxies which can be used to constrain the growth factor, $f(z)\sigma_8$, and the radial and angular distances to the sample (i.e., the $H(z)$ and $D_A(z)$ parameters). We used the LRG sample from the first two years of the eBOSS, denoted as DR14, to measure these parameters at the mean redshift of the survey ($z = 0.72$). We presented the first full-shape analysis of this sample (i.e. modeling Redshift-Space Distortions (RSD) simultaneously with an Alcock-Paczynski (AP) parametrization), and that should be followed up on and improved on once the full observational time of the eBOSS survey is completed for the final DR16 sample. The measured correlation function was decomposed into the first three non-zero multipoles of its Lagrange expansion, and compared with theoretical predictions made with a Convolution Lagrangian Perturbation Theory (CLPT) model combined with a Gaussian Streaming model (GS). We considered six free parameters, four RSD-parameters [$f, F', F'', \sigma_{F\sigma G}$] and two AP parameters [α, ϵ].

We tested our methodology using a set of 84 high-precision N-Series CutSky mocks built with BOSS-CMASS

properties. We fitted all individual mocks using two different methodologies: using only multipoles up to $\ell = 2$, and using all multipoles up to $\ell = 4$. The hexadecapole fits were computed in two different distance ranges, in the first we used the complete [28,124] $h^{-1}\text{Mpc}$ range for all of the multipoles, and in the second we cut out the smaller scales of the hexadecapole. This extends on previous works that performed this exploration using only the monopole and the quadrupole. The most accurate results are obtained from using the multipoles up to $\ell = 2$.

When including the hexadecapole we obtain a slightly smaller bias in the mean of the best fit values of the growth factor f , it goes from $|b_{f\sigma_8}| = 0.009$ (in the monopole quadrupole only case) to $|b_{f\sigma_8}| = 0.006$, however, given that the standard deviation also decreases the bias becomes more significant. The biases of the AP parameters also increase: α goes from a significance of 1.7σ to one of 2.5σ and ϵ from 0.5σ to 2.9σ . This behavior is related to the fact that the fits are driven by ϵ when we include the lower bins of the hexadecapole. The error bars for those lower scales are smaller, and therefore their constraining power is larger. This makes the accuracy of the model at small scales critical.

In order to characterize the statistical properties of the sample, especially its variance, we run our fitting methodology on two different sets of low-precision mocks with eBOSS properties: the QPM and EZ mocks. All of the mocks in both sets are fitted twice, the first considering only the multipoles up to $\ell = 2$, and the second with multipoles up to $\ell = 4$. The dispersion obtained from the two sets of low-precision mocks was fairly consistent in all cases and for all of the parameters of interest. However, the biases and distributions were not consistent with those obtained using high-precision mocks. The discrepancy arises because the GSRSD model can not match the multipoles of QPM/EZ mocks, thus no conclusion about the bias could be extracted from the fits. They will only be used as a reference for the variance of the best fits for eBOSS-like mocks.

The tests performed with mocks (high and low precision), demonstrated that the constraining power of the lower bins of the hexadecapole is large due to the smaller error bars of those points. We concluded that including the hexadecapole is desirable; however, it becomes critical to have accurate models, particularly of the small scales of the quadrupole and the hexadecapole. In this work, we adopted the conservative approach of excluding the hexadecapole in our fiducial methodology. We considered that even if the results with high-precision mocks validated fitting the hexadecapole with our model, the significance of the biases obtained using the hexadecapole are larger than those obtained only using monopole+quadrupole fits. Further work is required before including the hexadecapole with the CLPT+GSRSD

model on the LRG sample. Additionally, we did not have high-precision mocks with the properties of the eBOSS sample available (higher redshift and lower mean density) and we could not properly study the statistical properties of the fitting methodology with low-precision mocks.

Our final measurement was performed on the “combined” sample, using the fiducial methodology considering only the monopole and quadrupole. We constrained the logarithmic growth of structure $f\sigma_8 = 0.454 \pm 0.139$, $\alpha_{\parallel} = 0.954 \pm 0.151$ and $\alpha_{\perp} = 0.955 \pm 0.085$. The eBOSS DR14 LRG sample presents a large correlation in the large scale quadrupole that lies outside the 1σ variation observed in the mocks. This feature could be related to an unknown systematic effect or just a large statistical fluctuation. Given that we could not find any systematic that affects the quadrupole, and that a large fluctuation cannot be excluded, we analyzed the behavior of the fits when we eliminated those large scales in multipoles with $\ell \geq 2$ as a robustness test for our main result. Avoiding the latest three bins of the quadrupole achieves a significant improvement in the goodness of the fit to ~ 1 ; however the price paid is to eliminate the BAO information, which increases the degeneration of the parameters and biases the results, thus we lose information that constrains ϵ , and the contour regions become larger, giving more freedom to the fitter to move f to lower values.

We quote as our final cosmological constraint the logarithmic growth of structure multiplied by the amplitude of dark matter density fluctuations, $f(z_{eff})\sigma_8(z_{eff}) = 0.454 \pm 0.139$, and the Alcock-Paczynski dilation scales which allow constraints to be placed on the angular diameter distance $D_A(z_{eff}) = 1466.5 \pm 136.6(r_s/r_s^{fid})$ and the Hubble distance $H(z_{eff}) = 105.8 \pm 16(r_s^{fid}/r_s)\text{kms}^{-1}\text{Mpc}^{-1}$, where r_s is the sound horizon at the end of the baryon drag epoch and r_s^{fid} is its value in the fiducial cosmology at an effective redshift $z_{eff} = 0.72$. These measurements correspond to relative errors of 30.5%, 9.3%, and 15.1%, respectively considering the systematic error. Our results are consistent with previous measurements and with a Λ CDM model using Planck 2018 cosmology. Comparing our result with the forecasted ones, the measurements of $H(z)$, D_A and $f\sigma_8$ are respectively about 4, 2.9, and 2.4 larger than the predictions. This result might be caused by the non-uniform footprint in the current state of the survey, although the BAO DR14 LRG measurements also reported errors larger than the predictions (Bautista et al. 2018). We expect a reduction on the statistical error of a factor two by the end of the experiment for DR16 final analysis.

ACKNOWLEDGEMENTS

The authors thank Alejandro Áviles for the useful discussions over the model generation using CLPT-GSRSD.

MDIL acknowledges the support of a Durham University funded scholarship, part of the STFC funded Centre for Doctoral Training in Data Intensive Science at Durham University.

MV is partially supported by Programa de Apoyo a Proyectos de Investigación e Innovación Tecnológica (PAPIIT) No IA102516, NoIA101518, Proyecto Conacyt Fron-

teras No 281 and from Proyecto LANCAD-UNAM-DGTIC-319.

SF is supported by Programa de Apoyo a Proyectos de Investigación e Innovación Tecnológica (PAPIIT) No IA101619.

G.R. acknowledges support from the National Research Foundation of Korea (NRF) through Grant No. 2017077508 funded by the Korean Ministry of Education, Science and Technology (MoEST), and from the faculty research fund of Sejong University in 2018.

This project used the resources of DiRAC Data Centric system at Durham University, operated by the Institute for Computational Cosmology on behalf of the STFC DiRAC HPC Facility (www.dirac.ac.uk). This equipment was funded by BIS National E-infrastructure capital grant ST/K00042X/1, STFC capital grant ST/H008519/1, and STFC DiRAC Operations grant ST/K003267/1 and Durham University. DiRAC is part of the National E-Infrastructure.

This research used resources of the National Energy Research Scientific Computing Center, a DOE Office of Science User Facility supported by the Office of Science of the U.S. Department of Energy under Contract No. DE-AC02-05CH11231.

Funding for the Sloan Digital Sky Survey IV has been provided by the Alfred P. Sloan Foundation, the U.S. Department of Energy Office of Science, and the Participating Institutions. SDSS acknowledges support and resources from the Center for High-Performance Computing at the University of Utah. The SDSS web site is www.sdss.org. SDSS is managed by the Astrophysical Research Consortium for the Participating Institutions of the SDSS Collaboration including the Brazilian Participation Group, the Carnegie Institution for Science, Carnegie Mellon University, the Chilean Participation Group, the French Participation Group, Harvard-Smithsonian Center for Astrophysics, Instituto de Astrofísica de Canarias, The Johns Hopkins University, Kavli Institute for the Physics and Mathematics of the Universe (IPMU) / University of Tokyo, the Korean Participation Group, Lawrence Berkeley National Laboratory, Leibniz Institut für Astrophysik Potsdam (AIP), Max-Planck-Institut für Astronomie (MPIA Heidelberg), Max-Planck-Institut für Astrophysik (MPA Garching), Max-Planck-Institut für Extraterrestrische Physik (MPE), National Astronomical Observatories of China, New Mexico State University, New York University, University of Notre Dame, Observatorio Nacional / MCTI, The Ohio State University, Pennsylvania State University, Shanghai Astronomical Observatory, United Kingdom Participation Group, Universidad Nacional Autónoma de México, University of Arizona, University of Colorado Boulder, University of Oxford, University of Portsmouth, University of Utah, University of Virginia, University of Washington, University of Wisconsin, Vanderbilt University, and Yale University.

REFERENCES

- Abolfathi B., et al., 2017, preprint, ([arXiv:1707.09322](https://arxiv.org/abs/1707.09322))
- Alam S., et al., 2017a, *MNRAS*, **470**, 2617
- Alam S., et al., 2017b, *MNRAS*, **470**, 2617
- Alcock C., Paczynski B., 1979, *Nature*, **281**, 358

- Alonso D., 2012, preprint, ([arXiv:1210.1833](#))
- Anderson L., et al., 2014, *MNRAS*, **441**, 24
- Audren B., Lesgourgues J., Benabed K., Prunet S., 2013, *JCAP*, **1302**, 001
- Ballinger W. E., Peacock J. A., Heavens A. F., 1996, *MNRAS*, **282**, 877
- Bautista J. E., et al., 2017, preprint, ([arXiv:1712.08064](#))
- Bautista J. E., et al., 2018, *ApJ*, **863**, 110
- Blanton M. R., et al., 2017, *AJ*, **154**, 28
- Carlson J., Reid B., White M., 2013, *MNRAS*, **429**, 1674
- Chuang C.-H., Kitaura F.-S., Prada F., Zhao C., Yepes G., 2015, *MNRAS*, **446**, 2621
- Dawson K. S., et al., 2016, *AJ*, **151**, 44
- Eisenstein D. J., et al., 2005, *ApJ*, **633**, 560
- Fang W., Wang S., Hu W., Haiman Z., Hui L., May M., 2008, *Phys. Rev. D*, **78**, 103509
- Feldman H. A., Kaiser N., Peacock J. A., 1994, *ApJ*, **426**, 23
- Fukugita M., Ichikawa T., Gunn J. E., Doi M., Shimasaku K., Schneider D. P., 1996, *AJ*, **111**, 1748
- Gil-Marín H., et al., 2018, *MNRAS*, **477**, 1604
- Gunn J. E., et al., 1998, *AJ*, **116**, 3040
- Gunn J. E., et al., 2006, *AJ*, **131**, 2332
- Hartlap J., Simon P., Schneider P., 2007, *A&A*, **464**, 399
- Høg E., et al., 2000, *A&A*, **355**, L27
- Hou J., et al., 2018, *MNRAS*, **480**, 2521
- Joyce A., Jain B., Khoury J., Trodden M., 2015, *Phys. Rep.*, **568**, 1
- Kaiser N., 1987, *MNRAS*, **227**, 1
- Landy S. D., Szalay A. S., 1993, *ApJ*, **412**, 64
- Lewis A., Challinor A., Lasenby A., 2000, *ApJ*, **538**, 473
- Linder E. V., 2005, *Phys. Rev. D*, **72**, 043529
- Matsubara T., 2008, *Phys. Rev. D*, **77**, 063530
- Mueller E.-M., de Bernardis F., Bean R., Niemack M., 2014, preprint, ([arXiv:1408.6248](#))
- Perlmutter S., et al., 1999, *ApJ*, **517**, 565
- Planck Collaboration et al., 2016, *A&A*, **594**, A16
- Planck Collaboration et al., 2018, arXiv e-prints, [p. arXiv:1807.06209](#)
- Prakash A., et al., 2016, *ApJS*, **224**, 34
- Reid B. A., White M., 2011a, *MNRAS*, **417**, 1913
- Reid B. A., White M., 2011b, *MNRAS*, **417**, 1913
- Reid B. A., et al., 2012, *MNRAS*, **426**, 2719
- Riess A. G., et al., 1998, *AJ*, **116**, 1009
- Ross A. J., Percival W. J., Manera M., 2015, *MNRAS*, **451**, 1331
- Ross A. J., et al., 2017, *MNRAS*, **464**, 1168
- Rykoff E. S., et al., 2014, *ApJ*, **785**, 104
- Schlafly E. F., Finkbeiner D. P., 2011, *ApJ*, **737**, 103
- Sheldon E. S., et al., 2004, *AJ*, **127**, 2544
- Simpson F., Peacock J. A., 2010, *Phys. Rev. D*, **81**, 043512
- Smee S. A., et al., 2013, *AJ*, **146**, 32
- Sotiriou T. P., Faraoni V., 2010, *Reviews of Modern Physics*, **82**, 451
- Springel V., 2005, *MNRAS*, **364**, 1105
- Tegmark M., 1997, *Physical Review Letters*, **79**, 3806
- Tinker J. L., et al., 2012, *ApJ*, **745**, 16
- Vargas-Magaña M., et al., 2014, *MNRAS*, **445**, 2
- Wang L., Reid B., White M., 2014, *MNRAS*, **437**, 588
- White M., Tinker J. L., McBride C. K., 2014, *MNRAS*, **437**, 2594
- Wright E. L., et al., 2010, *AJ*, **140**, 1868
- Xu X., Padmanabhan N., Eisenstein D. J., Mehta K. T., Cuesta A. J., 2012, *MNRAS*, **427**, 2146
- Zarrouk P., et al., 2018, *MNRAS*, **477**, 1639
- Zhai Z., et al., 2017, *ApJ*, **848**, 76
- du Mas des Bourboux H., et al., 2017, *A&A*, **608**, A130

APPENDIX A: SELECTING PRIORS

As discussed in chapter 7, figure 17 shows that the $1\text{-}\sigma$ regions are fully contained inside our priors. However, the $2\text{-}\sigma$ regions are clearly cut by our prior to large values of ϵ . In this section we will discuss our reasons for not using larger ϵ priors in our analysis, as we will see prior selection was challenging giving the size of our errors.

Figure 18 shows a comparison between our final model and the multipoles of the data set, it is clear that the detection of the BAO signal is weak: the error-bars of the monopole have a similar size to the power of the BAO peak. This is problematic as the BAO peak locks the Alcock Paczynski parameters around a specific value. Given the limited capability of our methodology to fix the cosmology our model is vulnerable to being degenerated. As a consequence, we have to be very careful when choosing our priors as a large prior in the Alcock Paczynski parameters will result in degenerated regions contributing significantly to our statistics.

This is shown in figure A1 where we have run a second MCMC chain of our fiducial methodology but extending the priors of ϵ to $[-0.3, 0.3]$. These chains were done with a fixed value of $F2 = 0.0$ to save computational time as the goal of is not to obtain precise statistics but to show the effect of larger ϵ priors ($F2$ contributions to our model corresponds to second-order corrections on small scales, primarily broadening the parameter contours). The priors for the other parameters (i.e. neither ϵ nor $F2$) stay at the value quoted in table 8.

In figure A1, the blue contours show our default results, while the red ones show those with the enlarged priors on ϵ .

A second locus is present for large values of ϵ and small values of $f\sigma_8$. This second locus is centered somewhere around $f \approx 0.3$ assuming a nominal σ_8 value consistent with planck ($\sigma_8(z_{eff}) = 0.55$), which would result in the Alcock-Paczynski parameters switching the cosmology to $\Omega_M(z=0) \approx 0.03$ (for $\sigma_8(z=0) = 0.8$ and a flat universe, assuming that $f(z) \approx \Omega_M(z)^{0.6}$). This strongly disagrees with previous constraints made by Planck, that predicts a value of $\Omega_M(z=0) = 0.315 \pm 0.007$ (Planck Collaboration et al. 2018). Hence, the DR14 data does not allow us to broaden the priors too much, as the accuracy is not yet there in the data to rule out cosmological parameters already strongly rejected by Planck measurements.

Figure A2 shows why this secondary locus is chosen by our MCMC analysis to be an acceptable fit. The blue line is the median of the models of 100 points chosen randomly from the subset of MCMC points within the locus centered around $\alpha \approx 1$ and $\epsilon \approx 0$ (locus 1 in figure A1). The blue shaded regions indicate the 18th and 84th percentile confidence range. The red line and contours correspond to models randomly selected from points of our MCMC chain inside locus 2 (top panel of A1).

From figure A2 we observe that the best fit model within locus 2 do not show a well defined BAO peak. However, statistically, both sets of models are equally good and indistinguishable in terms of their likelihood. DR16 should have smaller errors around the BAO signal which could in principle discard this second solution (locus 2). As we have stated, this second locus is discarded using Planck CMB constraints, therefore we consider reasonable to choose priors on the Al-

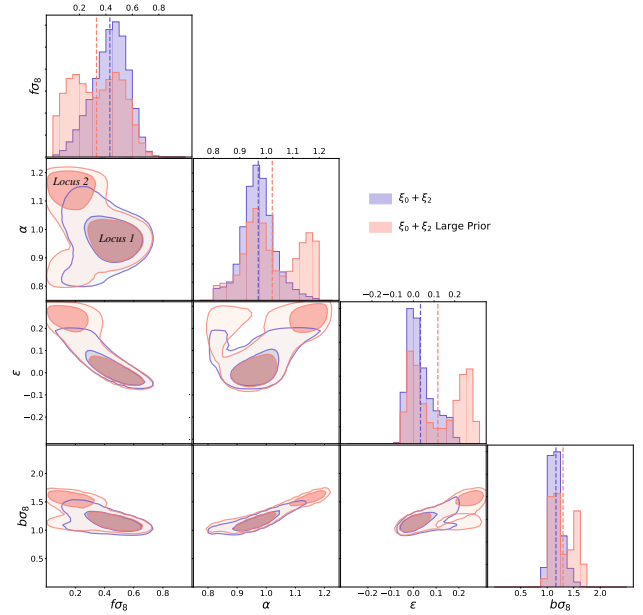


Figure A1. This plot is equivalent to Figure 17, here we presenting the MCMC chains of two fits to the RSD-AP parameters in the $\xi_0 + \xi_2$ space done with different priors in ϵ . The blue contours use the priors quoted in table 8 for all parameters but $F2$ that is set to zero. The red contours have larger priors on ϵ which are expanded to $[-3, 3]$ and also set $F2$ to zero.

cock Paczynski parameters that keep it out of our statistics. Considering mild Planck CMB constraints, it is reasonable to assume priors on α and epsilon of ± 0.2 around their nominal value, as Planck strongly rejects cosmologies that are beyond that alpha and epsilon range to several sigmas.

Figure A3 is included as a robustness test of our methodology, here our fiducial result is compared with a new MCMC chain computed reducing the priors of α to $[0.9, 1.1]$. As in A1 $F2$ is set to zero for both chains to save computational time. The plot shows that the α contours are cut by the new priors, nevertheless, the $1\text{-}\sigma$ contours of both chains are centered around the same values and have a similar shape, the main difference being marginally reduced size of the contours, which is expected when reducing the priors.

APPENDIX B: LIKELIHOODS FOR EBOSS SAMPLE USING HEXADECAPOLE.

In section 6.1 we applied our methodology to find the maximum likelihood fits of 84 Nseries high-resolution simulations. We have shown that our methodology provides consistent results with and without hexadecapole information. As stated in section 7 we decided to fit only the monopole and quadrupole, excluding the hexadecapole information, because the significance of the bias was better for this case. In this appendix, we show results including the hexadecapole.

We run two different chains that include ξ_4 using the combined data set (NGC+SGC). We use flat priors for our parameters; the range of these priors is the same as the one

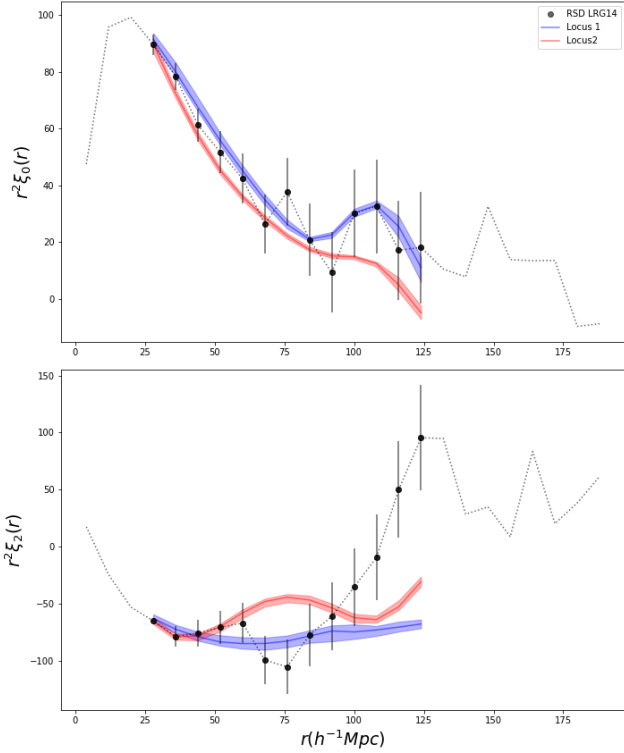


Figure A2. This figure shows the median and 1-sigma percentiles for 2 sets of 100 models built with 100 points chosen randomly from the subset of those explored by our MCMC. The blue contours correspond to points inside the peak centered around the expected cosmology ($\alpha \approx 1$ and $\epsilon \approx 0$). The red line and contours are computed with points inside the second peak that appears for large values of ϵ .

used for the main results are quoted in table 8. The statistical results of our parameters are quoted in table B1: the first line repeats for comparison purposes the results for monopole and quadrupole only ($\xi_0 + \xi_2$). The rest of the table includes the results using monopole, quadrupole, and hexadecapole ($\xi_0 + \xi_2 + \xi_4$). The second line uses the full $[28, 124] h^{-1}\text{Mpc}$ range in all multipoles. The last line, the monopole is in the $[28, 124] h^{-1}\text{Mpc}$ range, and the quadrupole and hexadecapole are in the $[28, 92] h^{-1}\text{Mpc}$ range, we cut out the large scales for the quadrupole and hexadecapole where potential systematic errors could be present. The results of $f\sigma_8$ and α are consistent in the fiducial ranges within $1 - \sigma$, for the two cases, $\xi_0 + \xi_2$ and $\xi_0 + \xi_2 + \xi_4$, but the ϵ values have a $1.4 - \sigma$ difference. Figure B1 shows the likelihood surfaces of the $\xi_0 + \xi_2 + \xi_4$ compared with our fiducial methodology ($\xi_0 + \xi_2$), they are both in the fiducial $[28, 124] h^{-1}\text{Mpc}$ range for all multipoles and both chains and they use the priors from table 8. The figure shows the $1-2\sigma$ confidence contours for the growth factor $f\sigma_8$, the linear bias $b\sigma_8$, the dilatation parameter α , and the warping parameter ϵ , together with their 1D distributions.

Figure 11, show that our hexadecapole data have a stronger amplitude on small scales that both sets of mocks. This mismatch in amplitude could be a problem of the mocks or could be due to a real signal in the data, or could be due to either an undetected systematic error in our data or a

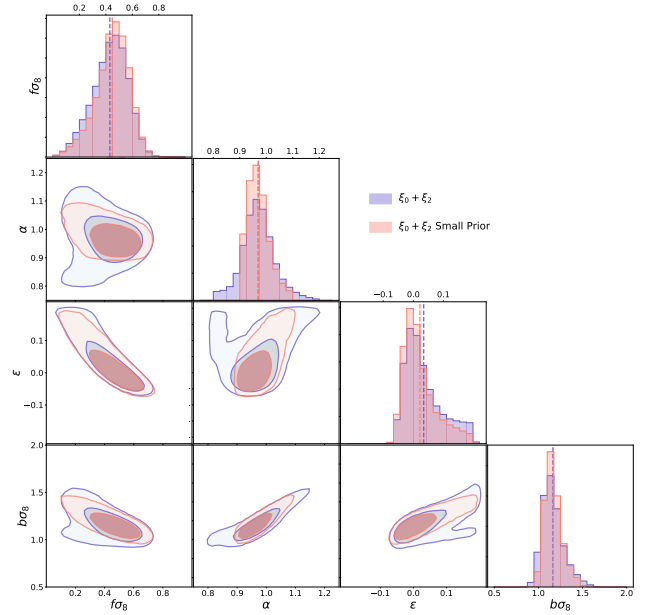


Figure A3. This plot is equivalent to Figure 17, here we presenting the MCMC chains of two fits to the RSD-AP parameters in the $\xi_0 + \xi_2$ space done with different priors in α . The blue contours use the priors quoted in table 8 for all parameters but $F2$ that is set to zero. The red contours have smaller priors on α which are reduced to $[0.9, 1.1]$ and also set $F2$ to zero.

statistical fluctuation. If it is the latter then the increase in data with DR16 should reduce this shift. If it is a real cosmological signature it should become more significant in DR16. Regardless of the origin of this larger amplitude, the MCMC fitter prefers a large value of ϵ and a small value of $f\sigma_8$ to fit the amplitude of the data hexadecapole (see Figure B1.).

Figure B1 shows that there is a secondary locus appearing for the smaller values of α , and that does not intercept with the $1-\sigma$ regions of the $\xi_0 + \xi_2$ fits. As in appendix A this second locus corresponds to a secondary solution that deviates from the Planck expected values and that is indistinguishable in terms of its likelihood. As in that section we suspect that this secondary locus is the consequence of the BAO signal not being able to fix the cosmology to a single value due to the size of the error bars. As we discussed in that section, DR16 should have smaller errors around the BAO signal which could in principle discard this second solution.

Figure B1 shows the results of cutting the large scales for the quadrupole and hexadecapole ($\ell = 2, 4$), the red contours come from a chain where the monopole is in the $[24, 128] h^{-1}\text{Mpc}$ range, and the quadrupole and hexadecapole in the constrained range of $[24, 92] h^{-1}\text{Mpc}$. When the last three bins of the quadrupole and hexadecapole are avoided we achieve a significant improvement in the goodness of the fit (we saw this same behavior in section 7 when removing the large scales of the quadrupole), we also lose the secondary locus that was present in the full approach; however, the price paid is to eliminate the BAO informa-

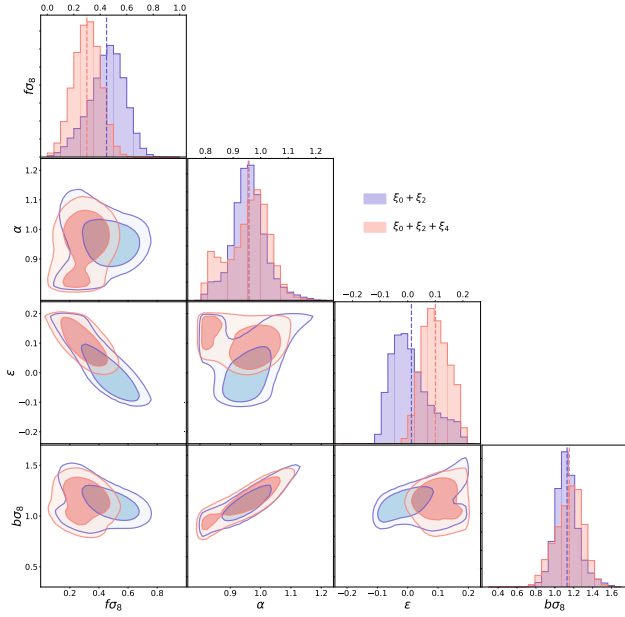


Figure B1. The shaded regions show the $1-2\sigma$ confidence surfaces found by our MCMC chains for the RSD-AP parameters for two cases: $\xi_0 + \xi_2$ (red) and $\xi_0 + \xi_2 + \xi_4$ (blue), all multipoles in both models are in the $[24, 128] h^{-1}\text{Mpc}$ range. The confidence contours for the growth factor $f\sigma_8$, the linear bias $b\sigma_8$, the dilatation parameter α , and the warping parameter ϵ are indicated, along with their 1D distributions. The dashed lines of each histogram are the mean values found by the MCMC chain.

tion. This increases the degeneration of the parameters and biases the results, we lose information that constrains ϵ and α , which in turn causes the contour areas to become larger, providing more freedom to the fitter to move f and α to lower values (Figure B2) and into the region that was a part of the secondary locus of the full range approach. The main impact of removing the large scales in the hexadecapole fits is in parameters that require the BAO peak to be constrained, as expected. When excluding the large scales, the BAO information is lost, and α is shifted in consequence.

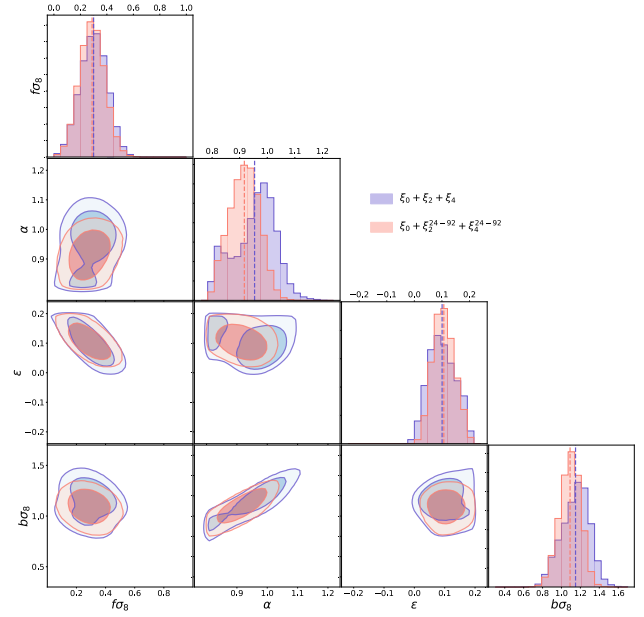


Figure B2. Similar to figure B1, here the red contours represent a fit where the quadrupole and hexadecapole are reduced to the $[28, 92] h^{-1}\text{Mpc}$ range while the monopole stays in the full range ($[24, 128] h^{-1}\text{Mpc}$), the blue contours show the fit where monopole, quadrupole and hexadecapole are in the full range.

Table B1. Results for the DR14 LRG sample. The first block is for our fiducial methodology, using the fiducial range for the $\xi_0 + \xi_2$ fit. The second block is for the $\xi_0 + \xi_2 + \xi_4$ fits in the ranges [24,128], [24,128], and [44,128] h^{-1} Mpc for their multipoles $\ell = 0, 2, 4$. The third block is for the $\xi_0 + \xi_2$ and $\xi_0 + \xi_2 + \xi_4$ fits when excluding the large scales for quadrupole and quadrupole/hexadecapole, respectively. The fiducial value for the $\sigma_8(z_{eff}=0.72) = 0.55$ (0.5495932). The eulerian bias is defined by $b = 1 + F'$.

Measurements with LRG sample DR14 Official Version.						
Case	$f\sigma_8$	$b\sigma_8$	$\langle F' \rangle$	σ_{FOG}	α	ϵ
$\xi_0 + \xi_2$ [28,124][28,124]	$0.454^{+0.119}_{-0.140}$	$1.110^{+0.116}_{-0.100}$	$2.2^{+3.8}_{-4.4}$	$3.7^{+3.0}_{-2.3}$	$0.955^{+0.055}_{-0.05}$	$0.000^{+0.090}_{-0.050}$
$\xi_0 + \xi_2 + \xi_4$ [28,124] [28,124] [28,124]	$0.29^{+0.10}_{-0.10}$	$1.14^{+0.14}_{-0.15}$	$-1.5^{+3.3}_{-3.1}$	$5.8^{+2.9}_{-3.2}$	$0.954^{+0.071}_{-0.092}$	$0.100^{+0.054}_{-0.049}$
$\xi_0 + \xi_2 + \xi_4$ [28, 124][28, 92][28, 92]	$0.285^{+0.093}_{-0.094}$	$1.079^{+0.108}_{-0.110}$	$-1.5^{+3.3}_{-3.0}$	$5.5^{+2.6}_{-2.8}$	$0.917^{+0.054}_{-0.056}$	$0.107^{+0.041}_{-0.039}$